A REVIEW OF METHODS FOR THE PREDICTION OF BVI NOISE

The BVI Working Group

F. Caradonna*, C. Kitaplioglu* & M. McCluer*
Army/NASA Rotorcraft Division
NASA Ames Research Center

J. Baeder & G. Leishman
University of Maryland

C. Berezin & J. Visintainer
Sikorsky Aircraft Division
United Technologies Corp.

J. Bridgeman
Flow Analysis Inc.
The Woodside Summit Group

C. Burley
NASA Langley Research Center

R. Epstein
The Boeing Company

A. Lyrintzis & E. Koutsavdis
Purdue University

G. Rahier & Y. Delrieux
ONERA

J. Rule & D. Bliss
Duke University

ABSTRACT

This paper compares aeroacoustic methods for the prediction of parallel blade-vortex interaction noise using data from a specialized rotor test. The test, performed in the NASA Ames 80- by 120-Foot Wind Tunnel, involved a small-scale rotor interacting with a vortex generated by a wing mounted upstream. These data were the focus of an informal working group that compared a wide range of methods for the prediction of BVI noise. The aerodynamic models include computational fluid dynamics, boundary element, and analytical methods. Acoustic methods include Kirchhoff methods and the Ffowcs-Williams Hawkings approach. The comparisons of computed and measured surface pressure data reveal a number of differences, none of which seem to have major acoustic significance. Comparisons of computed and measured far-field pressures show that BVI acoustics is generally well predicted with more differences being found between the Kirchhoff methods. Within the limitations of the present test, this indicates that BVI noise is reasonably well predicted when vortex parameters (location, circulation, and core radius) are accurately known.

* organizers

Presented at the American Helicopter Society Technical Specialists' Meeting for Rotorcraft Acoustics and Aerodynamics, Williamsburg, VA, October, 1997.

NOMENCLATURE

α_v	angle of attack of the vortex generator
c	rotor blade chord
C	vortex generator chord
Γ	non dimensional vortex strength
μ	advance ratio
M_{tip}	tip Mach number
R	blade radius
r	radial position
r_a	blade vortex radial core size
r_c	vortex generator radial core size
V_θ	tangential velocity
U_∞	free stream velocity

INTRODUCTION

Rotor-vortex interactions have been the subject of many experimental, analytical, and computational studies. Most of this activity is motivated by the importance of blade-vortex interaction (BVI) as a major source of rotorcraft noise and vibration problems. BVI is also of basic computational interest because it is a well-defined problem encompassing several important numerical issues of rotorcraft aerodynamics. For example, the computation of vorticity convection, the resulting unsteady loads on an airfoil, and the ensuing pressure waves, are all involved in modeling BVI. The conceptual simplicity of the problem has encouraged the development of numerous computational methods, ranging from simple, incompressible 2-D analyses to full 3-D, Euler/Navier-Stokes computational fluid dynamics (CFD) codes. However, experimental data of comparable simplicity was unavailable due to the difficulty of generating sufficiently clean vortices in a wind-tunnel environment, and also of acquiring corresponding loading and acoustic data. These experimental problems have been largely solved by the rotor/vortex-generator approach originally employed by McCormick[1] and later developed into a full aeroacoustic test at the Ames Research Center.[2] Figure 1 is a photograph of the rotor and vortex generator in the Ames wind tunnel set up. The data obtained from this latest test was suitable for evaluating computational models and has become the focal point for the present study.

Most of the methods presented herein used a specified initial vortex form that is derived from a separate related test by McAlister and Takahashi.[3] The accompanying acoustic methods employ either a Ffowcs-Williams Hawkings (FWH) or Kirchhoff approach. These methods are mainly compared with data from a near-miss vortex interaction, but head-on (zero miss distance) results are also included.

The present work cannot be viewed as a definitive comparison of results, because most methods are still under active development. Nevertheless, the results obtained to date are extensive. They provide a means to assess the adequacy of the data and also serve as a focus for comparing and summarizing the range of methods that constitute our probable future aeroacoustic analysis and design tools.

THE BVI EXPERIMENT AND DATA

A rotor model was tested in the acoustically treated NASA Ames 80- by 120-Foot Wind Tunnel for the purpose of studying the isolated, parallel blade-vortex interaction. This experiment used a simple blade geometry and an externally generated vortex to provide an uncomplicated flow environment for computational code validation. This arrangement permitted control of the vortex parameters (strength, sense and location) independently of the rotor state. The rotor was operated at zero thrust, so that the influence of its own wake would be minimized. Figure 2 shows a schematic of the experimental set-up. This figure illustrates how the vortex blade separation distance and the vortex sense of rotation were independently controlled by the height and angle of the vortex generator.

Facility

The NASA Ames Research Center 80- by 120-Foot Wind Tunnel is part of the National Full-Scale Aerodynamics Complex (NFAC) located at Moffett Field, California. The wind tunnel is acoustically treated with 6 inches of foam on the walls and ceiling and 10 inches on the floor. The maximum velocity in the test section is 100 knots, and the axial turbulence intensity is less than 0.5%.[4] This large facility allowed the small-scale experiment to be minimally affected by wall reflections or flow turbulence.

Rotor Geometry

The two-bladed, teetering rotor had a diameter of 7.125 feet. The blades were untwisted with a rectangular planform. The blades employed a NACA 0012 profile with a constant 6-inch chord. The hover tip Reynolds number was approximately one million at a tip Mach number of 0.7. Each blade had 30 absolute pressure transducers (on either the upper or lower surface) that were arranged in three equal chordwise arrays. Figure 3 shows the pressure transducer distributions on the blade. The main blade structure was carbon/epoxy composite, and very stiff in bending and torsion to eliminate aeroelastic effects. Full cyclic pitch and collective pitch control were provided through a swashplate. The rotor was operated at zero thrust to minimize self-generated tip vortices. It was always trimmed to zero flapping to enable repeatable control of the blade-vortex miss distance. The rotor rotated clockwise as viewed from above.

Vortex Generator

A streamwise vortex was generated directly upstream of the rotor by a vertically oriented, semi-span wing (NACA 0015 airfoil section, 18-inch chord). The Reynolds number for the vortex generator wing was approximately 600,000. The vortex generator (VG) was equipped with a telescoping tip that permitted remote placement of the streamwise vortex at any desired location with respect to the rotor plane. This vertical distance between the vortex and the rotor blade was measured by a stroboscopic video camera. The visualization was performed by ejecting smoke from the tip of the vortex generator and illuminating a cross-section of the vortex with a laser sheet (located at 0.876R). Figure 2 illustrates the blade-vortex vertical proximity, Z_V, and the vortex generator angle of attack, α_V. The streamwise distance between the trailing edge of the vortex generator and the rotor blade tip at 180° azimuth was 48" or 2.67 VG chords. The tip vortex strength and structure were not directly measured in this experiment. Therefore, it was necessary to infer this information from a previous experiment. The process of obtaining this information is described later.

Microphones

There were seven, 1/2-inch diameter, Bruel & Kjaer microphones located in the test section: two in the near-field and five in the far-field. The microphones were calibrated every day using a standard pistonphone. Both near-field microphones were located 12 inches (2 rotor chords) below the rotor, at the 87.6% rotor radius. Figure 4 shows the position of the near-field microphones relative to a rotor blade. Figure 5 shows the location of microphones 1 through 5 on the traverse.

Experimental Test Matrix

The test matrix included a range of hover tip Mach numbers, vortex generator angles, and different vortex locations. Most of the data were obtained at an advance ratio of about 0.2 for each hover Mach tip number by adjusting the flow velocity. Table 1 shows the high Mach number subset of data that were acquired. The majority of the computational results in this paper are for a single test case. Blade loads and acoustics were computed for Case 1D where test conditions were: hover tip Mach number, M_{tip} = 0.715, advance ratio, μ = 0.198, angle of attack of vortex generator, α_V = -12 deg, and separation distance between the vortex and the blade, Z_V/c = -0.25. This case was chosen because of its simplicity (the blade does not pass through the vortex or its trailing sheet). A few additional comparisons were also made with a "head-on" case (Case 1B), where the vortex-blade separation distance was zero.

Acoustic Data

The Acoustic Laboratory Data Acquisition System (ALDAS)[5] was used for acoustic data acquisition and reduction. Experimental acoustic data were digitized at 1024 points per rotor revolution on a Macintosh-based, four-channel, 16-bit A/D data system. All incoming data were low-pass filtered at 10 kHz to prevent aliasing errors. Thirty rotor revolutions of data were acquired for each test condition. The data were averaged based on a rotor one-per-revolution trigger signal. The experimental data underwent a thorough review to check for data corruption, consistency, and repeatability.

Blade Surface Pressure Data

A 32-channel, 16-bit digital data acquisition system acquired the 60 channels of blade

pressure data in two sets. One transducer was duplicated between the two sets to check repeatability. The data were acquired at 1024 points per revolution and anti-alias filtered at 10kHz. Thirty-two revolutions of data were recorded and were ensemble averaged using the rotor 1/rev. There was no degradation by the averaging process because the data were highly repeatable.[6] Maximum deviations from the average pressure were small, (less than 5%) and this occurs mainly at the vortex/leading edge impact time. This probably indicates that the signal variation is due to slight vortex wander.

The resulting averaged data were accessible by a graphics/analysis program that provided displays in the form of either time-histories or chordwise pressure distributions. The data can be filtered to display any desired spectral components. This filtering was useful for eliminating unexplained low frequencies and biases in the data. For display of timewise data, the lowest four harmonics were filtered in both the data as well as all of the computed results.

Data Quality

An essential goal of the experimental work was to obtain simultaneous surface pressure and far-field acoustic data of suitable quality for code validation. The pressure and acoustic data were subject to independent filtering and averaging processes and it was necessary to assure that they were consistent with each other. A first check of consistency was to assure that similar data trends (for instance, pressure vs. vortex proximity) were obtained for both the transducers and microphones. This level of checking revealed no data problems. It did, however, reveal a probable error in the vortex proximity.[7] It was found that for $\alpha_V = +12°$, the rotor-vortex miss distance, Z_V, was in error by approximately 0.125 chord. This has been accounted for in the values of Z_V/c in Table 1.

Figures 6 and 7 show typical blade pressure and acoustic time histories over a portion of a revolution near the BVI event. Both of the figures show the time histories as bands of data which indicate the individual records with the highest and lowest levels. This provides an indication of the experimental error. For blade pressures the error is approximately 2.5% of the maximum peak-to-peak value. For acoustics, the error is approximately 10% of the maximum peak-to-peak value.

VORTEX STRUCTURE AND MODELING

The computational methods used in the present investigation require a good representation of the vortex structure. Unfortunately, this vortex structure could not be measured in the present experiment. However, extensive vortex structure data had been previously obtained[3], using laser Doppler velocimetry, in an experiment performed in the NASA Ames/Army 7- by 10-Foot (No.2) Wind Tunnel (7-by 10). The 7-by 10 experiment used a vortex generator that was identical to that used in the present test. Tip vorticies shed by the 7- by 10 vortex generator were measured one, two, four, and six generator chords downstream. These data have been used to study the functional form (algebraic and exponential forms[8] have been studied) of the vortex and the critical parameters that charcterize the functions (circulation and core size).

The present approach to characterizing the vortex is to find a model which agrees with measured circulation and peak velocity (magnitude and location). It was found that the initially reported values of circulation (0.35) and core size (0.05) do not seem to produce a good match with both the measured circulation and peak velocity from Ref. 3. This necessitated a more extensive study of the vortex. The ensuing discussion shows that an algebraic vortex core model (often referred to as the "Scully" model) provides the best overall fit with the measured vortex structure. With this model the tangential velocity equation is expressed in dimensionless form by:

$$V_\theta(r) = \frac{\Gamma}{2\pi} \frac{r}{\left(r_a^2 + r^2\right)}$$

where r_a is the nondimensional vortex core size, and the nondimensional variables are defined as;

$$V = \frac{\bar{V}}{U_\infty}, \quad \Gamma = \frac{\bar{\Gamma}}{U_\infty C}, \quad r = \frac{\bar{r}}{C}$$

Several approaches were taken to determine the "best" values for the circulation and core radius. In the first approach (by J. Bridgeman), values of core radius and circulation were chosen to provide the exact location and magnitude of the peak velocity in the vortex. This approach had produced excellent results in an earlier investigation.[9] Vortex velocity data at two and four generator chords downstream (the approximate location of the interaction) were used. The computed values for nondimensional circulation and core size using this approach with the algebraic core model were 0.416 and 0.054, respectively. Figure 8 shows the resulting comparison with the tangential velocity data. This figure also includes the results of applying this procedure to an exponential core. It is seen that only the algebraic model gives both the correct velocity peak and circulation.

In an alternate approach (by G. Leishman), circulation and core size values were chosen which provided a best least squares (for the algebraic model) fit at each of four downstream measurement locations. Figure 9 shows the fit at one of these locations. These values were averaged and the resultant values of nondimensional circulation and nondimensional core radius were 0.373 and 0.045, respectively.

Both of the above approaches to fitting the data provide excellent comparisons. While this again demonstrates the effectiveness of the algebraic vortex model, the two methods produce different values of vortex circulation. The important issue, however, is to have a good value for the vortex generated in this BVI test rather than in the earlier 7- by 10 test. Due to differences in the wind tunnel characteristics and test set-ups there is no reason that the two circulation values should be the same .

An additional method for determining vortex parameters was subsequently employed (by J. Bridgeman). This approach was to use the blade pressure data as an indirect velocity probe. In this approach the FPX code was used to predict the rotor blade loading for Case 1D. (Here, the miss distance is one quarter-chord and the core size is not a significant factor. Thus, the core size of 0.054 was used, but is not critical in this case.) As the leading-edge pressure time history is an indicator of the vortex structure, the circulation was varied until the predicted peak pressure differential at x/c = .02 made a best fit to the measured pressure variation. The value of circulation was determined to be 0.374 , which is very close to the value obtained for the latter least squares fit. The working group decided to use a circulation of 0.374 and a core radius of .054 for most of the ensuing computations. The validity of this approach depends on the ability to perform an *a priori* prediction of the leading edge pressure variations. The effectiveness of this approach will be verified by the comparisons of the various computations.

SUMMARY OF COMPUTATIONAL METHODS

The basis for all the acoustic prediction methods is either an implementation of the Ffowcs-Williams Hawkings equation (without the quadrupole term) or the Kirchhoff approach. Because the latter method requires flow-field data, it is only used in combination with a CFD method. The FWH approach only requires surface pressure data and can be used with any aerodynamic method. With one exception, the computational effort required by the near-field aerodynamics is much greater than that of the acoustics. Furthermore, there are many more aerodynamic than acoustic prediction methods. Therefore, the following contributors are listed roughly in the order of increasing complexity of the aerodynamic model.

Method 1. Experimental Data Input to FWH (WOPWOP)

Acoustic predictions were performed by C. Burley[8] at NASA Langley Research Center using measured blade pressures as input to the rotor acoustic prediction code WOPWOP.[10] The measured chordwise blade pressures input were those obtained at the 3 radial stations (r/R = .772, .876, .946). Acoustic predictions were made for both far-field microphones and near-field microphones.

The WOPWOP code is based on the acoustic formulation 1A of Farassat.[11] This formulation is a time-domain representation of the Ffowcs Williams-Hawkings equation, excluding the volume source or "quadrupole" term. Since high speed impulsive noise is substantially shock-formation related, it is not accounted for in the formulation; neither are volume source effects of transonic BVI. Formulation 1A was developed to predict discrete frequency noise of helicopter rotors at subcritical speeds, and is valid for arbitrary blade motion, geometry and observer location. The WOPWOP code predicts thickness and loading noise at a specified observer location. These noise sources are blade surface terms.

The noise calculation in WOPWOP starts by dividing the rotor blade surface into a number of chordwise and spanwise acoustic source panels. A numerical integration is then performed over each panel to accurately determine, from the blade shape and surface pressures, its overall contributions to the noise at a given observer location. For computational efficiency, it is assumed that the integration over each panel may be approximated by using the integrand value determined at the panel center which would be representative of the entire panel area. Therefore the code computes the panel center and then numerically estimates the contribution to the noise from a given panel per desired observer time.

Some variations of computational input were studied. A spanwise grid which matched that of the measured data (from approximately r/R=.75 to r/R=1.0), was compared to a spanwise grid which extended much farther inboard than that of the measured data (from r/R=0.3 to r/R=1.0). The computational spanwise grid was adjusted to locate the measured data at the center of the surface panels. The number of spanwise panels was varied from 10 to 50 between approximately r/R=.75 and the tip (r/R=1.0) to check for numerical differences that may occur due to grid size. No significant difference in the predicted acoustics was seen. The chordwise computational grid was also varied, from 27 chordwise locations to 54. Again no significant difference in the predicted acoustics was seen. Finally the number of time steps used in the computation was varied from 256 to 1024 time steps per blade passage. The maximum level of the BVI peak for all the acoustic time histories increased by less than 3 Pascals, and the computation time approximately tripled. The final computational grid consisted of 50 radial panels (between r/R = 0.75 and r/R=1.0), 27 chordwise panels, and 256 time steps per blade passage (1/2 revolution). Linear interpolation of the measured data onto the computation grid was used for the chordwise, spanwise and azimuthal (time) directions. The particular configuration of this BVI experiment (rectilinear vortex and parallel interaction) makes possible this simple interpolation.

Method 2. Indicial Method with FWH

The indicial approach provides a fundamental method of finding the time-dependent aerodynamic response to a wide range of unsteady flow conditions. If the indicial response can be found for a specified unit input, such as a step change in angle of attack or the penetration of a sharp-edge gust, then the unsteady aerodynamic response to an arbitrary input can be found by Duhamel superposition. The indicial response in some cases is known analytically, in other cases numerically, and it can also be found experimentally by inverse techniques. If the linearity of the flow physics over the required range of conditions can be justified, then one advantage of the indicial method is a tremendous saving in computational cost over performing separate flow field calculations. By using certain analytic forms of the indicial response, efficient numerical procedures can be developed to solve the Duhamel integral. Such a method, developed by Leishman[12] at the University of Maryland, obtains a generalized exponential function that closely approximates the exact two-dimensional solution for lift on an airfoil penetrating a sharp-edged gust in subsonic flow. This allows the unsteady lift for any non-convecting gust field to be computed extremely efficiently. The resulting method can then be applied to obtain the time-varying lift variation on the rotor in response to a specified inflow. For the present application, this inflow is obtained from the tangential velocity induced by the generator vortex. To provide an input to the FWH equation for the acoustics solution, the predicted unsteady lift over the rotor blade

is used to synthesize an equivalent surface pressure distribution using thin-airfoil theory. A novel and very efficient binning technique is used to track the times of emission and reception at the observer locations, thereby preserving the overall efficiency of the approach. Thickness noise effects are incorporated into the acoustics solution using a standard source/sink model.

Method 3. Singularity Method with Cloud-in-Cell Vortex Model (ARHIS), and FWH (PARIS)

Another singularity method, called ARHIS[13] has been developed by G. Rahier at ONERA. The method is incompressible and is based on the use of vortex elements. This method models the interacting vortex as a freely convecting and deforming cloud of vortex elements. Subsonic compressibility effects are included by means of Prandtl-Glauert corrections combined with local thickening of the airfoil. In addition, finite span effects are introduced through an elliptic-type correction of the pressure coefficients. This is the only method used in this paper that models vortex deformation. This particular near-field computation is coupled to an acoustic code, called PARIS[14], which employs a time-domain formulation of the FWH equation. The blade is discretized into 10 radial sections and the whole aerodynamic/acoustic computation (ARHIS+PARIS) requires about 1 minute on a CRAY Y-MP for the cases studied here.

Two distributions of vortex elements have been used for this study, with the standard values of the circulation and core radius. The first one is axisymmetrical and provides a velocity field corresponding to the standard algebraic vortex model. Computations using this model are referred to as Method 3B. The second contribution is an attempt to account for the fact that the vortex is probably not fully rolled up. It is not axisymmetrical and its outer region roughly emulates a vortex sheet.[15] However, the total circulation is the same as for the axisymmetric vortex. This leads to a maximum induced velocity a little lower (-14%) than the maximum velocity induced by the standard algebraic vortex model. Computations using this model are referred to as Method 3A.

Method 4. Singularity Method

The fastest near-field flow computations are the 3-D methods built around non-singular distributed Greens function elements that model the airfoil, its wake, and the interacting vortex. A three-dimensional boundary element method has been employed at McDonnell Douglas Aerospace and Duke University by Epstein and Rule[16,17]. The aeroacoustic boundary element method is unsteady and compressible, based on the convective wave equation (linearized potential equation), and employs a Lagrangian convection of the vortex. The computation applies the boundary element method using Analytical/Numerical Matching (ANM) in conjunction with Turbulent Core Model vortex dynamics (TCM). ANM is a hybrid scheme combining a low-resolution global numerical computation with a high-resolution local analytical calculation to form a composite solution. ANM avoids the subtlety involved in singular integral equations and their numerical implementation. TCM vortex dynamics is based on the fundamental integral conservation laws of the aerodynamic flow field, and offers a real flow vortex model which has no empirical free parameters. The current implementation does not include free distortion of the vortex. A Mach number weighting scheme is used to account for blade rotation effects as calculations were not done in a rotating reference frame.

Method 5. Full-Potential CFD Method (FPR) and FWH (WOPWOP)

Method 5 was submitted by Berezin[18] of Sikorsky Aircraft Division of United Technologies Corp. The incorporation of transonic, three-dimensional effects requires the discretization and numerical solution of some form of the full flow equations. The potential equations are the simplest such equation set, because they only solve for mass conservation with energy conservation being expressed by the Bernoulli equation. The full-potential CFD code, FPR, has been coupled with the well-known WOPWOP code[10] at Sikorsky in order to predict the far-field acoustic field of the BVI. These computations use a compact grid of about 46,000 nodes and proceed in time steps of 0.25 degrees. The grid normal boundaries are about 5 chords from the blade surface. The BVI computations are initiated with a steady

solution at an azimuth of 90 degrees and the solution then marches to a final azimuth of 270 degrees. The computation requires 1.3 CPU hours on an IBM RS6000 Model 590 workstation.

Method 6. Full-Potential CFD Method (FPX) and Kirchhoff

Near-field modeling of the BVI has also been performed using the FPX code (a later development of FPR) by Bridgeman[19] at the Army Aeroflightdynamics Directorate (AFDD). The method uses a density-biased central difference discretization that is solved by an approximate factorization scheme. This code employs a blade-fixed, stacked O- or H-grid, with the former being used for the present application. The passing vortex is modeled by inclusion of its specified flow field (including the vortical core) as a component of the total velocity. This component becomes a forcing function to the equation. The specified vortex-induced velocity component also adds a forcing term to the boundary condition - this term, when used alone, is the well-known "transpiration condition". In the present model, the vortex structure is specified and there is no distortion mechanism. This grid is identical to that used for the Method 5 FPR computations and the solution should also be nearly identical. The main difference between FPR and FPX, for the options exercised for the present computations, is that the former requires approximately twice the CPU time.

The Kirchhoff method is used to compute the far-field noise. The surface integral of the non-linear solution in the near-field gives enough information for the analytical calculation of the far-field. Pressures and pressure derivatives from the near-field CFD calculation are interpolated onto a surface that completely encloses the rotor blades.

A rotating Kirchhoff surface, which has the advantage of allowing the use of the same computational mesh as the CFD calculations, is typically located several chord lengths away from, and completely surrounds, the blade surface. The Farassat and Myers formulation[20], which allows both rotation and translation of the Kirchhoff surface, is used for the calculations.

Method 7. Euler CFD Method (TURNS) and Kirchhoff

The structured-grid Euler/Navier-Stokes code, TURNS[21] has been applied, in combination with a Kirchhoff code, by John Bridgeman as well as several other authors in this study.

The TURNS code uses Roe's upwind-biasing in all three directions with a high-order MUSCL-type limiting on the right-hand-side. An LU-SGS (Lower-Upper Symmetric Gauss Seidel) implicit operator is chosen. An early version of TURNS[22] was modified by Baeder and Srinivasan[23] to compute the BVI noise of an isolated rotor blade interacting with an upstream-generated vortex. The vortex is incorporated in a quasi-steady manner using a field velocity approach. This modification also permitted the computation of a perturbation about a specified vortex structure without numerical dissipation. The resulting solution is valid for any interaction where the vortex structure is not deformed. The interaction in this study displayed no obvious viscous features and did not require the full Navier-Stokes analysis (in this or any of the subsequent TURNS applications). Assuming adequate grid resolution, all nonlinear effects on the acoustic propagation were accurately modeled within the framework of the Euler equations.

Method 8. Euler CFD Method (TURNS)

The TURNS code was used by McCluer[24] of NASA Ames Research Center for a comparison of near field acoustics for eight different test conditions. This method used direct computation to obtain pressure time histories and therefore results were only available for the near-field. These were earlier computations that used a nondimensional vortex strength of 0.35 and a vortex core radius of 0.05.

Method 9. CFD Methods (TURNS and FPR) coupled with Kirchhoff and FWH (WOPWOP)

9a. TURNS and Kirchhoff with nonstandard vortex model

9b. TURNS and Kirchhoff with standard vortex model

9c. FPR and Kirchhoff with standard vortex model.

9d. TURNS and FHW with standard vortex model

TURNS was used by Lyrintzis and Koutsavdis[25] of Purdue University to compute the aerodynamic field close to the helicopter rotor. Full potential computations using the FPR[26] code to calculate the blade surface pressure distributions were performed to compare to the Euler results. A Kirchhoff surface which rotated with the blade was used to predict far-field acoustics. Acoustic results using the WOPWOP code are also included.

Method 10. Euler CFD Method (TURNS) and FWH

A similar version of TURNS was used by Baeder[27] of the University of Maryland, to predict the far-field pressure with a FWH acoustic computation. Unsteady computations with ten Newton-like subiterations per time step provide second-order time accurate solutions. A FWH method similar to that of Method 2 was used to calculate thickness and loading noise in the far-field.

DISCUSSION OF AERODYNAMIC RESULTS

Case 1D

Figures 10 through 13 show a comparison of measured and computed azimuthal surface pressures variations for the basic Case 1D using the following five methods (see Tables 1 and 2):

3. Singularity, boundary element with freely deforming vortex (Rahier)
4. Compressible Singularity method, boundary element (Rule)
5. FPR full-potential (Berezin)
6. FPX full-potential (Bridgeman)
7. TURNS Euler (Bridgeman)

Most contributions to these comparisons include both aerodynamic and acoustic results. Aerodynamics results are not available for all methods (but obviously were performed, since these are required for the acoustics). Method 7 used the same code (TURNS) as methods 8 - 10, and is therefore representative of all the Euler CFD computations for the same values of vortex core size and circulation.

Figures 10 - 13 show the pressure time histories at x/c = 0.02, 0.11, 0.40 and 0.83 for the upper and lower surfaces at 88% radius. (This particular radius is chosen, because it is typical of all radii, but is far enough from the tip to permit comparison with two-dimensional methods.) For these methods, chordwise pressure distributions are also shown and compared with the data in figures 14 - 19. In the time history plots, the first four harmonics are filtered out and the curves are offset to separate the different chordwise methods.

Methods 3 represent the only computations in this study that model the freely deforming wake (i.e. that have a force-free wake model). The specified vortex structure is an initial condition and is free to vary subsequently. These particular computations are also unique in that they employ two initial vortex models, the standard vortex model (method 3B) and a non-axisymmetric model with a total circulation equal to that of the standard model (method 3A). The latter model has been used because the proximity of the vortex generator to the rotor makes it probable that the vortex is, in fact, not fully developed. It is seen in figures 10 - 13 that the comparison of the 3A results is very good from the leading edge to the trailing edge. The main differences with the data are toward the trailing edge (especially on the upper surface) where the computed BVI pulse occurs sooner than that in the data. This probably results from the fact that the computation is incompressible and all signals propagate at infinite speed. The compressibility correction used does not correct phase errors. (On the lower surface, this phase error is not seen at the rearmost chordwise location. This effect is not understood.) These phase errors are not of acoustic significance because they represent errors of propagation of weak acoustic sources rather than generation errors. The primary acoustic generation region is at the leading edge region and the comparisons there are very good. For method 3B, employing the standard axisymmetric initial vortex structure, the comparisons at the leading edge are not as good. This latter computation shows a tendency to overpredict the peak pressures at x/c = .02. In addition, this model also shows greater deviation from the measured pressures at the end of the BVI-induced pressure jump (on both upper and lower surfaces). This deviation is also seen at x/c = .11. However, at the other chordwise locations the comparison is quite

good. In this case, the comparisons of chordwise pressure distributions (Figs. 14 & 15) do not give a clear picture of the difference between the two vortex models. The distributions at indices 492, 512, and 522 show no clear differences between the models. This is an accident of the particular time indices chosen. Overall, both of the computations used here are quite good with the non-axisymmetric vortex model producing the better results.

Method 4, the compressible boundary element computations using the standard vortex model, shows very good comparison with the upper surface pressure variations at the frontmost chordwise locations, except at the conclusion of the BVI-induced pressure jump (very similar to method 3B). Toward the trailing edge, the computed BVI pulse is noticeably broader than that in the data. On the lower surface the peak BVI-induced pressure slightly exceeds the measured value at $x/c=0.02$, but underpredicts noticeably at $x/c = 0.11$. All other lower surface comparisons are quite good except for the previously mentioned pulse broadening that occurs toward the trailing edge.

The comparison of chordwise pressure distributions, Fig. 16, is very good. The separation of upper and lower surface pressures that occurs at the end of the BVI-pulse (caused by pressure waves of opposite sign originating near the leading edge) is seen to be exaggerated in the computations. It is clear in these figures that the surface element density at the trailing edge is quite sparse.

Methods 5 and 6, the full-potential computations, also compare well with the data. The upper surface BVI peak pressure is well predicted. The previously mentioned pressure variation overprediction (at the end of the BVI pulse) also occurs here, but with a much diminished amplitude. The lower surface BVI pressure peak is slightly underpredicted. On the lower-surface, midchord region (Fig. 12) the computed BVI-induced pressure pulse is much sharper than seen in the data. (Actually all of the computations are sharper in this region, but the effect is exaggerated here.) The pressure pulse that occurs near the trailing edge (Fig. 13) is well predicted, but the computations then show another pulse of opposite sign that is not seen in the data. This effect appears related to the passage of the vortex past the trailing edge.

The comparison of computed and measured chordwise pressure distributions (Figs. 17 & 18) is quite good. The comparisons at and prior to the peak pressure point are excellent. Following this peak point (index 522) there are more differences from the experimental data and this is seen with many of the other methods as well. The differences at this point are due to slight phasing errors between the computed and actual vortex location. Since the timewise pressure gradients are very high at this point, slight location errors cause large differences when viewed in the chordwise distributions. Therefore, the differences seen here are not significant. At index 542, the pressure comparison is very good except at the trailing edge. The difference is more emphasized in Method 5, which is probably due to a larger time step being used. This is probably related to the fixed-wake sheet that is used in all standard potential models (analytical or numerical). One would expect this to also occur in Method 4. That this is not seen clearly with Method 4 may be due to the sparse grid that is used. The comparisons for the leading-edge region, which is the primary acoustics source, is good.

Method 7 is the first of three Euler/TURNS results. The Euler results seen in Figs. 10 - 13 appear very similar to the previous full-potential results, with the exception that the mid-chord lower-surface pressures match better with the data and the leading-edge pressures slightly underpredict the pressure peaks. The chordwise pressure variations (Fig. 19, index 532 and 542) shows a separation of upper and lower surface pressures (occurring at the end of the BVI-pulse) that is similar to that seen with Method 4.

The comparison between Methods 6 and 7 (FPX and TURNS) leading-edge pressure variations provides reasonable substantiation of the deduced vortex circulation value. The general agreement between the methods (especially for the initial part of the BVI) and the good agreement with the data indicate that the deduced standard vortex model is adequate for the present purpose.

Case 1B

Limited computations were also performed for the head-on interaction, Case 1B. The point of this exercise is to shed additional light on the aerodynamic methods used and the BVI phenomena by pushing them to extremes. Figures 20 through 23 show comparisons for three different methods (Methods 3A, 6 and 7). Figures 24, 25 and 26 show the chordwise pressure distributions at various times during the BVI interaction. Of the three methods, only Method 3 models the bifurcation and deformation of the vortex as it impacts the leading edge. The other two methods merely impose the undisturbed vortex velocity field on the flow field as it passes by the rotor.

The Method 3A boundary-element results compare well, overall, with the data. However, it is found that Method 6 and 7, despite their vortex approximations, compare as well. The full-potential result is especially good (such comparisons for head-on interactions are previously seen in Ref. 9). In fact, it is surprising that the head-on BVI comparison (Case 1B) appears to be closer than the near-miss case (Case 1D). Only the trailing edge pressures at index 542 (Fig. 25) show a serious discrepancy, and this has no relevance to BVI noise. Method 7 (Fig. 26) also shows serious differences in the latter stages (that is, the propagation stages) of the BVI process. Overall, the comparisons of the computed and measured pressure data are quite good for all methods.

These results suggest that, while there are aspects of BVI that clearly require improvement (especially near-field propagation and related loads) the BVI wave generation process is amenable to many types of analyses. However, this evaluation must await a comparison of the above methods based on a more objective measure of the effects of the various flow models. A comparison of acoustic computations and measurements is required.

DISCUSSION OF ACOUSTIC RESULTS

All of the methods listed in Table 2 provided calculations of the acoustic field. Method 8 provided only near-field results, while Methods 6, 7, and 9A - 9C provided only far-field results. Some selected calculations for a "head-on" interaction (Case 1B) are also included. The computed acoustic time histories for the various methods compared to the averaged data are shown in Figures 27 - 39. Microphone #3 was chosen to represent the acoustic far-field, and microphone #7 represents the near-field. Only a portion of a full revolution near one of the BVI pulses is shown on each figure.

Method 1

The acoustic predictions computed by WOPWOP using the measured blade pressures are compared to measured acoustic time histories in Figs. 27 and 28 for two run conditions (Cases 1D and 1B). The predictions for two different input methods, described previously, are shown as solid or broken lines and the measured data is shown as a dashed line.

For spanwise sources distributed r/R = 0.75 to 1.0, the predictions of the maximum peak level at the far-field microphone (Microphone 3) for both cases (Case 1D and Case 1B) are lower than the measurement. However, the comparison of the character of the predicted pulses, particularly their width, is in very good agreement with the measurements. The predictions for the near-field microphone (Microphone 7) also show very good agreement with the measurement. The positive peak level compares well; however the negative peak for both cases is underpredicted on the order of 20%. Note also the presence of a "bump" on the falling edge of the BVI pulse distinctly evident in the far-field data, somewhat more prominent for the head-on interaction, Case 1B. This feature is quite faithfully, if somewhat exaggeratedly, reproduced by these computations.

Since the measured data were obtained for a parallel interaction, the vortex contacted the blade for nearly the full span. However, the acoustic predictions included only the outer 75% of the blade. Thus noise sources on the inner part of the blade were not considered in the predicted acoustics. This may explain why the peak amplitudes between measured and predicted acoustics do not match. The measured data show the peak-to-peak blade pressures at r/R=.876 and .772 to be nearly the same. From

this it is conjectured that possibly the measured pressures at r/R=.772 could be used in WOPWOP to define the inboard blade loading. Thus, the pressures at r/R=.772 were used to define the inboard loading to r/R=0.3. The predicted acoustic results are shown in Figures 27 and 28 for Cases 1D and 1B, respectively. Of course this is an overestimation, since the velocity inboard is decreasing and the pressures due to the vortex interaction will be less, assuming this is a truly parallel interaction. The comparisons of predicted and measured acoustics for these cases are, in general, improved. The predicted peak pressures are in better agreement in amplitude and phase with the measurement. In addition to not having the full spanwise blade loading defined, differences in the acoustic predictions may also be attributed to the lack of pressure data at the leading edge of the blade. Some of the leading edge pressure transducers were inoperable during the test. To 'fill' in for these missing data, the pressure data at these x/c locations were either substituted with interpolated data or replaced with data from an adjacent transducer. Since BVI occurs over a very short time and is known to be a leading edge phenomenon, the acoustic predictions are sensitive to the accuracy of the pressures and their derivatives, particularly those at the leading edge.

Methods 2, 3, and 4

These methods use some form of either indicial or singularity analysis as indicated on Table 2 and described previously. The results are shown in Figures 29-33. In the near-field (Microphone 7), Methods 3B and 4 obtain very good agreement with the data; the former slightly overpredicts while the latter slightly underpredicts. Method 2 has some difficulty in the development of the near-field. This is attributed to assumptions regarding approximation of the acoustic near-field.

In the far-field (Microphone 3), Method 2 does very well, the near-field approximations being no longer important. Method 4 captures the magnitude of the BVI pulse quite well; however, the pulse width and shape are somewhat distorted. Method 3B significantly overpredicts the BVI pulse amplitude. When the non-axisymmetricvortex model is then used in Method 3A, the results are much improved with a good match of the pulse amplitudes in the far-field.

Figure 31 shows results for the head-on interaction (Case 1B) using Method 3A. Both near- and far-field acoustic results are reasonably good. The prominent "bump" on the falling edge of the positive pulse in the data, while not at all reproduced in the far-field, is present in the near-field calculation.

Method 5

Method 5 is a full-potential calculation of the blade pressures coupled with a FWH-type calculation of the acoustic field. The results are shown in Fig. 34. This method somewhat underpredicts the near-field. However, the far-field results indicate excellent agreement with the data.

Methods 6 and 9C

These methods couple full-potential calculations with Kirchhoff method calculations of the acoustic field. The results (available only for the far-field) are shown in Figures 35(a) and 38(d) respectively. The results are remarkably similar with the same characteristic large negative pulse as well as underprediction of the positive pulse. Method 9C also includes a second positive pulse of amplitude roughly one third that of the primary positive pulse. Note that while Method 5 uses an identical aerodynamic computation as Method 6, the acoustic predictions differ considerably.

Method 6 also provides a calculation of the head-on interaction (Case 1B) which shows features similar to those of Case 1D. The prominent "bump" on the falling edge of the positive pulse seems to be reasonably faithfully reproduced by the calculation (Fig. 35(b)).

Method 8

Figure 37 shows the result of a direct Euler calculation of the near-field and shows good correlation with the data, successfully capturing the pulse width and pulse shape but slightly overpredicting the amplitude.

Methods 9D and 10

These methods couple Euler calculations of the blade pressures with FWH-type computations of the acoustic field. The results, in Figs. 38(e)

and 39, show excellent agreement with data in the far-field. Method 9D shows a slight underprediction of the first negative peak and a slight overprediction of the second negative peak, while the positive peak is matched very well. As with Method 5, the near-field is somewhat underpredicted.

Methods 7, 9A, and 9B

These methods couple Euler calculation of the blade pressures with Kirchhoff calculation of the acoustic far-field. Methods 7 and 9B both utilize the standard vortex model which presumably results in the same blade pressures. The positive pulse is predicted quite well, while a prominent negative pulse, similar to the one observed with Methods 6 and 9C (full potential + Kirchhoff) and not present in the data, is also present. Method 9A, which utilizes a slightly different vortex model, shows some slight improvement in correlation with data over Method 9B.

Near-field results using Method 9A (Fig. 38 (b)) overpredict the data somewhat as was seen with Method 8. In contrast with Method 10, note that the pulsewidth is significantly wider than the data.

Figure 36(b) shows a calculation of the head-on interaction (Case 1B) using Method 7. Correlation with data similar to Case 1D (Fig. 36 (a)) is seen. However, note that the falling edge "bump" seems to be completely absent.

All of these methods are summarized in Figs. 40 where the peak-to-peak values of the first BVI pulse (left side - rising, right side - falling, for far-field Microphone 3) are shown for the experimental data as well as for each calculation method, grouped by acoustic method and by aerodynamic method. Error estimates for the experimental data are indicated.

In general, all the methods correlate well with the far-field data, but a number of noticeable differences are seen. The quality of the FWH acoustic comparisons is directly related to that of the surface pressure comparisons. The CFD methods all compare equally well with the surface pressures and this is reflected in excellent far-field acoustic comparisons. The non-CFD methods also produce very good results, with the indicial method being one of the best. The results from the Kirchhoff methods are more complex. These exhibit a large negative pulse not seen in the data. Moreover, the far-field acoustic results do not correspond as closely with the quality of the surface pressure comparisons. The Euler/Kirchhoff methods (TURNS) produces better comparisons than the potential/Kirchhoff. This may indicate that the CFD far-field accuracy is not simply related to that of the surface solution.

The differences seen here between the euler/ and potential/Kirchoff are not presently understood. It has been verified, for at least one of the potential/Kirchoff implementations, that these particular solutions are not strongly dependent on the Kirchhoff surface location (for the locations presently used, which ranges from 0.5 to 2.0 chords outboard from the tip). This may not necessary exclude the possibility of an outer boundary condition effect. Another possibility is that there may be significant differences in the dissipation of pressure waves between these euler and potential methods. This suggests a need for more detailed investigation of the flow fields of these solvers and future comparisons with the near-field microphone data.

There does appear to be a clue to the possibility of numerical acoustic dissipation differences. Recall that the surface pressures reveal a downstream propagating wave that manifests itself as a momentary separation between the upper and lower surface pressures. This is most clearly seen in the head-on interaction, case 1B (see figures 24, 25, and 26; index number 532). These figures also show the computations using the panel, potential and euler methods. The latter two methods, being compressible, clearly display the downstream wave. However, the Euler method shows a much stronger wave than the potential result. A similar result is also seen for case 1D. Figures 16, 18, and 19 show comparisons with the compressible-panel, potential and Euler methods. The wave-induced pressure separation is much weaker in this case. However, the computations all clearly show the effect, with the Euler solution being the strongest. These differences may be indicative

of major differences in the acoustic dissipation properties of the methods - and this could be a cause of the differences seen in the Kirchhoff results. However, it is too early exclude other possible explanations for these observations. We do not understand, for instance, why the euler method seems to overpredict the strength of the downstream wave.

In spite of such questions, it is clear that there is a very good ability to predict the acoustics of the parallel BVI.

CONCLUDING REMARKS

This paper has considered two simple parallel BVI interactions, a near-miss case and (to a more limited extent) a direct-hit case, and determined that the pressure and acoustic data (together with the inferred vortex model) are a suitable basis for the initial validation of computational models. A user of this data should expect to obtain reasonable comparisons with these blade surface and acoustic data before proceeding on to compute more complex interactions.

Present comparisons with these data use a variety of analytic, boundary-element and CFD methods to predict the aerodynamics and these are combined with FWH or Kirchhoff methods for predicting the acoustics. Most of these methods employ a common, fixed vortex form and trajectory. Most of these methods predict all the blade surface pressure characteristic features of the interaction including the initial pressure jump followed by a downstream moving wave that reflects upstream from the trailing edge. This clear wave behavior in the near-field is unusual and indicates a degree of unsteadiness that far exceeds that found in most flows for which the aerodynamic methods are normally used. Under these conditions it is not surprising that differences do occur in some of the computational results. However, these differences occur mainly after the primary pressure jump (which occurs when the vortex is adjacent to the leading edge), which is the primary event of acoustic importance. This primary pressure jump appears to be well predicted by all methods and one should expect to obtain good comparisons with acoustic predictions obtained from these results.

Nevertheless, differences do occur between the various acoustic computations. Generally, excellent results were obtained using the FWH (with all aerodynamic methods). A greater variability of results was obtained from the Kirchhoff methods. These differences may be partly due to the particulars of implementation. (It should be noted that these methods are still in a state of active development.) However, it is also possible that many of these differences are related to far-field inaccuracies of the CFD solvers - in spite of their having good surface solutions. It should also be noted that the present results are not a complete compilation of Kirchhoff methods - notably the non-rotating Kirchhoff approach is not included. One should also note that the present interactions show no sign of nonlinearity and the FWH approaches are therefore the methods of choice. Higher speed cases involving flow nonlinearity were not performed in this test. For such cases, Kirchhoff methods may have clear advantages.

The present comparisons required a vortex whose structure had to be inferred from a combination of testing (in another facility) and computations. The resulting axisymmetric vortex model is undoubtedly not a complete description of the actual vortex, which (because of its age) may not be fully formed. In fact, one of the present methods did employ a non-axisymmetric vortex model (in addition to the standard model) and did obtain improved results. At this point it cannot be positively said whether such differences are a result of the vortex model or the solution implementation. Clearly, there is much work to be done in the area of determining the actual vortex structure. These vortex structural considerations are especially important for direct interactions. (However, the results obtained for the head-on interactions are unexpectedly good.) Nevertheless, the present vortex model gives acceptable results with all methods and should be considered to be, at least, a good starting point for future validation computations based on this data.

It should be recalled that the vortex core radius in this experiment does not, probably, match the core radius of interacting vortices in

an actual operational BVI encounter. It would be interesting to study the influence of the core size on the aerodynamics and acoustics of BVI events. Further testing to include various core sizes would be far more complicated and costly than the present test. It should still be possible, however, to investigate parallel BVI of various cores by computational means. Two dimensional computations using an extremely fine grid resolution should be able to capture all the essential physics. Such computations could be lengthy, but the physical insight gained thereby would allow us to modify our existing methods (if necessary) to model the complete range of interactions.

It should also be recalled that the parallel BVI is only a small subset of the possible range of blade-wake interactions. Oblique interactions deserve at least as much consideration as parallel BVIs. These interactions occur on a longer time-scale and can be as important for vibrational as for acoustic reasons.

One of the most interesting results obtained is the fact that the simplest methods worked so well compared to far more complex models. Of course, the present BVI is intrinsically simple and only acoustic applications are being considered. Full rotor-wake computations wherein loads and performance must be predicted (in addition to acoustics) cannot be expected to yield so easily to the simplest approaches. Nevertheless, for particular, well-understood solution requirements, it is clear that great simplifications can be made.

Overall, excellent results were obtained, indicating that a significant capability exists to predict the BVI interaction and its acoustic implications. This does not imply, however, that the acoustic problem is solved. In this test the vortex location was well known and the vortex structure was fairly well-defined. In a full rotor computation, however, these are not known to a great degree of accuracy and the ability to predict these is probably the greatest challenge for the future.

REFERENCES

[1] McCormick, B.W., and Surendraiah, M., "A Study of Rotor Blade-Vortex Interactions" The 26th Annual Forum of the American Helicopter Society, Washington, D.C., June 1970

[2] Kitaplioglu, C. and Caradonna, F. "Aerodynamics and Acoustics of Blade-Vortex Interaction Using an Independently Generated Vortex" AHS Aeromechanics Specialists Conference, San Francisco, CA, January 1994.

[3] McAlister, K. W., and Takahashi, R. K., ``NACA 0015 Wing Pressure and Trailing Vortex Measurements,'' NASA TP 3151, November 1991.

[4] Zell, Peter T. "Performance and Test Section Flow Characteristics of the National Full-Scale Aerodynamics Complex 80- by 120-Foot Wind Tunnel," NASA Technical Memorandum 103920, January 1993.

[5] Watts, M.E., "ALDAS User's Manual", NASA Technical Memorandum 102831, April 1991.

[6] Kitaplioglu, C. and Caradonna, F. "A Study of Blade-Vortex Interaction Aeroacoustics utilizing an Independently Generated Vortex" AGARD Symposium, Berlin, Germany, October 1994.

[7] Kitaplioglu, C., Caradonna, F. X. and Burley, C. L., "Parallel Blade-Vortex Interactions: An Experimental Study and Comparisons With Computations," Proceedings of the American Helicopter Society 2nd International Aeromechanics Specialists' Conference, Bridgeport, CT, October 1995.

[8] Gallman, J, Tung, C, Schultz, K.J., Splettstoesser, W.R., Buchholz, H., Spiegel, P., Burley, C.L., Brooks, T., Boyd, D.D., "Effect of Wake Wake Structure on Blade-Vortex Interaction Phenomena: Acoustic Prediction and Validation," 1st CEAS/AIAA Aeroacoustic Conference, Munich, Germany, June, 1995.

[9] Caradonna, F.X., Strawn, R.C., and Bridgeman, J.O., ``An Experimental and Computational Study of Rotor-Vortex Interactions,'' Fourteenth European Rotorcraft

Forum, Milano, Italy, September 20-23, 1988. Also, see Vertica, Vol. 12, No. 4, pp. 315-327, 1988.

[10] Brentner, K.S., "Prediction of Helicopter Rotor Discrete Frequency Noise" NASA TM 87721, October 1996.

[11] Farassat, F.; and Succi, G.P.: "The Prediction of Helicopter Rotor Discrete Frequency Noise" Vertica, Vol. 7, No. 4, 1983, pp. 309-320

[12] Leishman, J.G., "Subsonic Unsteady Aerodynamics Caused by Gusts Using the Indicial Method" Journal of Aircraft, Vol. 33, No. 5, Sept.-Oct. 1996.

[13] G. Rahier, "Modelisation de l'interaction profil tourbillon en fluide parfait et application au rotor d'helicoptere" La Recherche Aerospatiale (with abridged version in English), No. 4, pp. 241-252, July 1995.

[14] P. Spiegel, "Prevision et analyse du bruit emis par un rotor principal d'helicoptere en presence d'interactions pale-tourbillon" ONERA Publication 1996-1, February 1996.

[15] Rahier, G., and Delrieux, Y., "Influence of Vortex Model in Blade-Vortex Interaction Load and Noise Predictions," American Helicopter Society Technical Specialists' Meeting for Rotorcraft Acoustics and Aerodynamics, Williamsburg, VA, October 1997.

[16] Epstein, R.J., Rule, J.A., and Bliss, D.B., "A Novel Method for Calculating Two-Dimensional Blade Vortex Interactions," AIAA Journal, Vol. 35, No. 5, May 1997.

[17] Rule, J.A. and Bliss, D.B., "Prediction of Turbulent Trailing Vortex Structure for Rotorcraft Blade-Vortex Interaction," Proceedings of the 51st Annual Forum of the AHS, Fort Worth, Texas, May 1995.

[18] Torok, M. and Berezin, C., "Aerodynamic and Wake Methodology Evaluation Using Model UH-60A Experimental Data," Journal of the American Helicopter Society, Vol. 39, No. 2, April 1994.

[19] Bridgeman, J.O., Ramachandran, K., Caradonna, F.X., and Prichard, D.S., "A Computational Analysis of Parallel Blade-Vortex Interactions Using Vorticity Embedding," 50th Annual Forum of the American Helicopter Society, Washington, DC, May, 1994.

[20] Farassat, F. and Myers, M.K., "Extension of Kirchhoff's Formula to Radiation from Moving Surfaces," Journal of Sound and Vibration, Vol. 123, No. 3, 1988, pp. 451-461.

[21] Srinivasan, G. R., and Baeder, J. D., ``TURNS: A Free-Wake Euler/Navier-Stokes Numerical Method for Helicopter Rotors,'' AIAA Journal, Vol. 31, No. 5, May 1993, pp. 959--962.

[22] Srinivasan, G. R., ``A Free-Wake Euler and Navier-Stokes CFD Method and its Application to Helicopter Rotors Including Dynamic Stall,'' JAI Associates Inc., TR 93-01, November 1993.

[23] Baeder, J. D., and Srinivasan, G. R., ``Computational Aeroacoustic Study of Isolated Blade-Vortex Interaction Noise,'' presented at the AHS Aeromechanics Specialists' Meeting, San Francisco, CA, January 1994.

[24] McCluer, M. S., "Helicopter Blade-Vortex Interaction Noise with Comparisons to CFD Calculations," NASA Technical Memorandum 110423, December 1996.

[25] Lyrintzis, A. S., Koutsavdis, E. K., and Strawn R. C., "A Comparison of Computational Aeroacoustic Prediction Methods," Proceedings of the 2nd AHS International Aeromechanics Specialists' Conference, Vol. 1, Bridgeport, CT, Oct. 1995, pp. 3-58 - 3-69.

[26] Xue, Y. and Lyrintzis, A.S., "Rotating Kirchhoff Formulation for 3-D Transonic Blade-Vortex Interaction Hover Noise," AIAA Journal, Vol. 32, No. 7, July 1994, pp. 1350-1359.

[27] Khanna, H. and Baeder, J.D., "Coupled Wake/CFD Solutions for Rotors in Hover," 52nd Annual Forum of the American Helicopter Society, Washington, DC, June 1996.

Table 1. Experimental Test Matrix.

CASE	Run/Point	M_{tip}	μ	Z_v/c	α_v
1A	50/12, 52/07	0.715	0.198	+0.25	-12°
1B	50/08, 52/06	0.714	0.198	0.0	-12°
1C	50/07	0.714	0.198	-0.125	-12°
1D	50/06, 52/08	0.715	0.198	-0.25	-12°
2A	49/10	0.716	0.198	+0.125	+12°
2B	55/06	0.714	0.198	0.0	+12°
2C	49/11, 55/08	0.715	0.198	-0.125	+12°
2D	55/07	0.715	0.198	-0.25	+12°

Table 2. BVI Aeroacoustic Prediction Methods.

METHOD NUMBER	AERODYNAMIC MODEL	ACOUSTIC METHOD	VORTEX MODEL	AUTHOR
1.	Experimental data input	FWH (WOPWOP)	n/a	Burley
2.	Indicial Method	FWH	Std	Leishman
3.	Singularity method, 2-D (ARHIS)	FWH (PARIS)	Cloud-in-cell free vortex a) non-axisym. b) Std	Rahier
4.	Singularity method, 3-D	FWH	Std	Epstein/ Rule
5.	Full potential CFD (FPR)	FWH (WOPWOP)	Std	Berezin
6.	Full potential CFD (FPX)	Kirchhoff	Std	Bridgeman
7.	Euler CFD (TURNS)	n/a	Std	Bridgeman
8.	Euler CFD (TURNS)	direct computation	Γ=0.35, r_a=0.050	McCluer
9.	a) Euler CFD (TURNS) b) Euler CFD (TURNS) c) Full-Pot. CFD (FPR) d) Euler CFD (TURNS)	(a-c) Kirchhoff, blade-fixed surface d) FWH (WOPWOP)	a)Γ=0.35,r_a=0.050 b) Std c) Std d) Std	Lyrintzis
10.	Euler CFD (TURNS)	FWH	Γ=0.35, r_a=0.050	Baeder

where Std = Standard Vortex Model: $V_\theta(r) = \frac{\Gamma}{2\pi r}\frac{r^2}{\left(r_a^2 + r^2\right)}$ where $\Gamma = 0.374$, $r_a = 0.054$

Figure 1. Photograph of BVI experiment in the NASA 80- by 120-Foot Wind Tunnel.

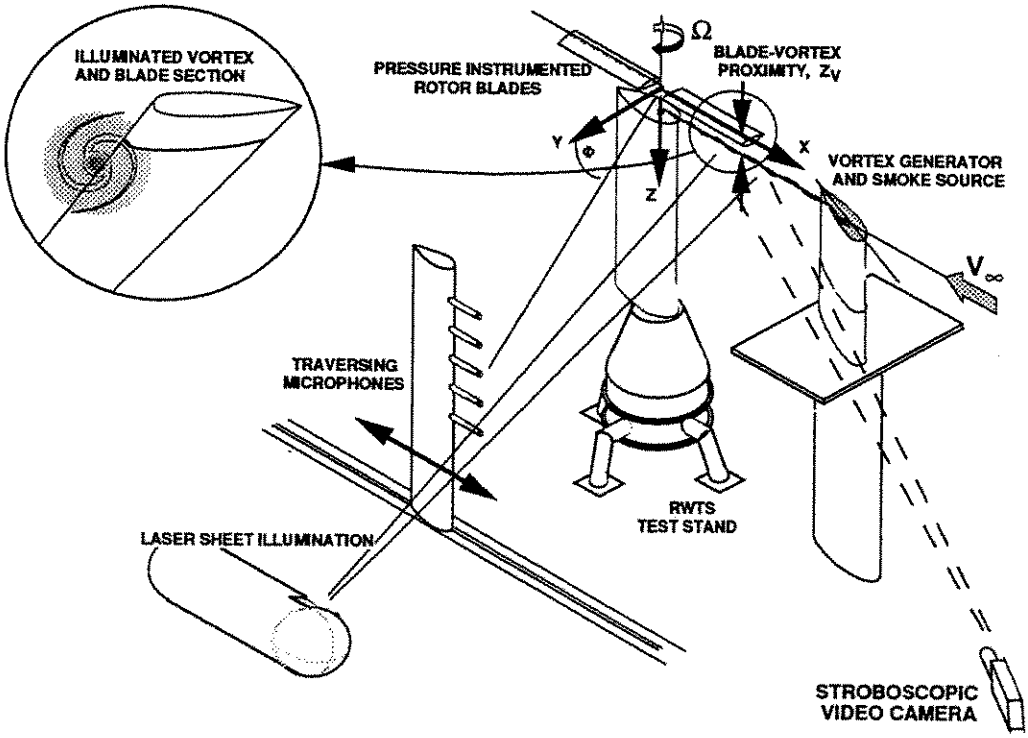

Figure 2. Schematic of experimental set up.

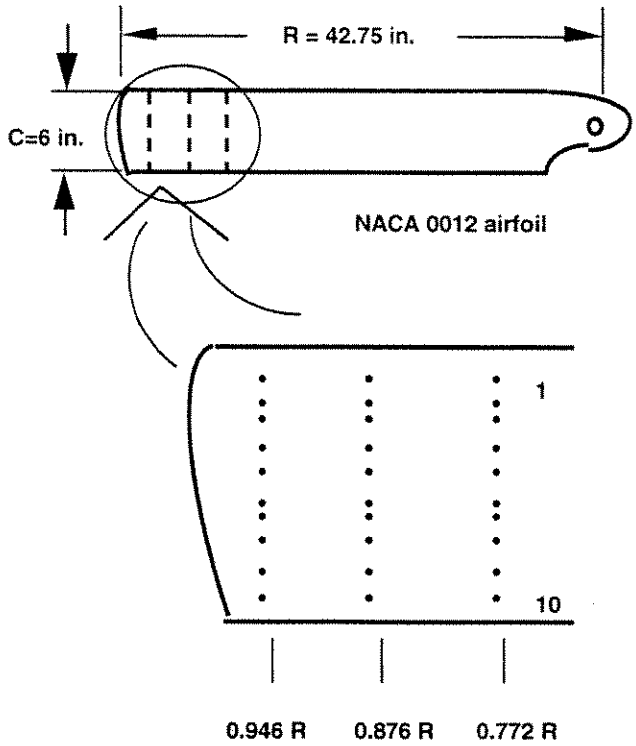

Transducer	Chordwise position
1	0.02
2	0.11
3	0.20
4	0.31
5	0.40
6	0.48
7	0.56
8	0.64
9	0.72
10	0.83

Figure 3. Blade pressure transducer distribution.

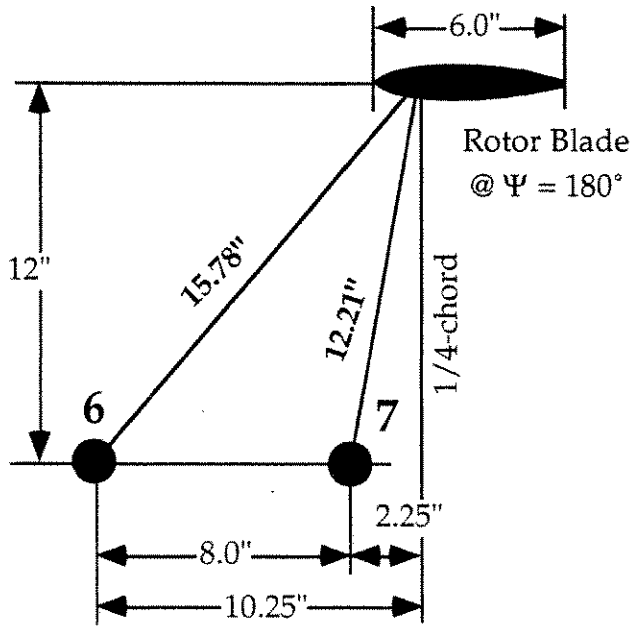

Figure 4. Schematic of the position of the near field microphones relative to the rotor.

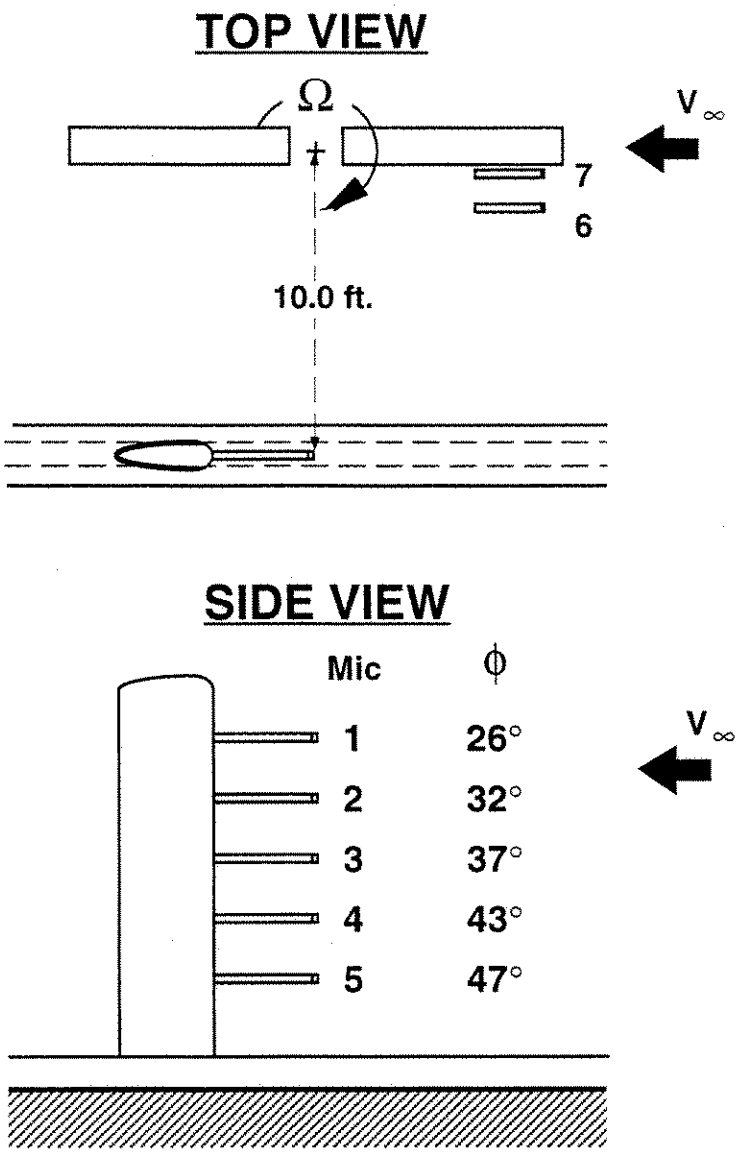

Figure 5. Position of microphones on traverse relative to rotor.

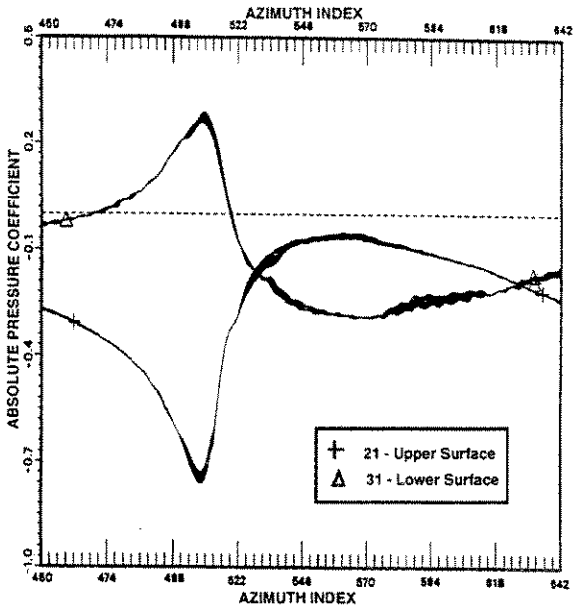

Figure 6 Experimental Variation in Unfiltered Absolute Surface Pressure Coefficient for Case 1d, x/C = 0.02, Leading Edge Transducers 21 and 31, over 32 samples.

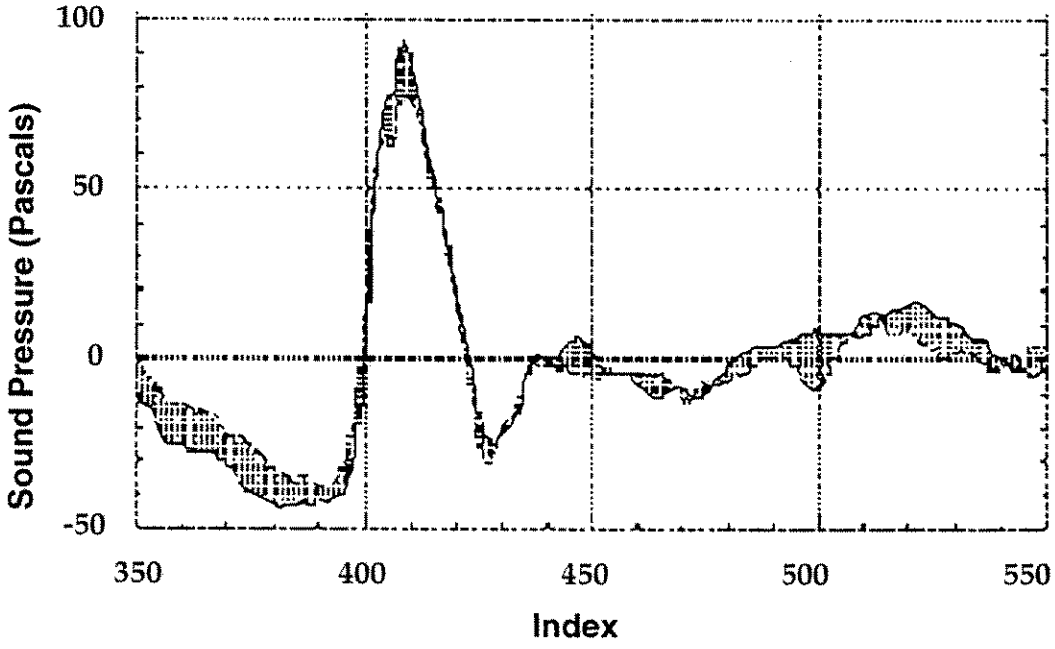

Figure 7. Experimental Variation of Acoustic Data for Case 1D, microphone 3, over 32 samples.

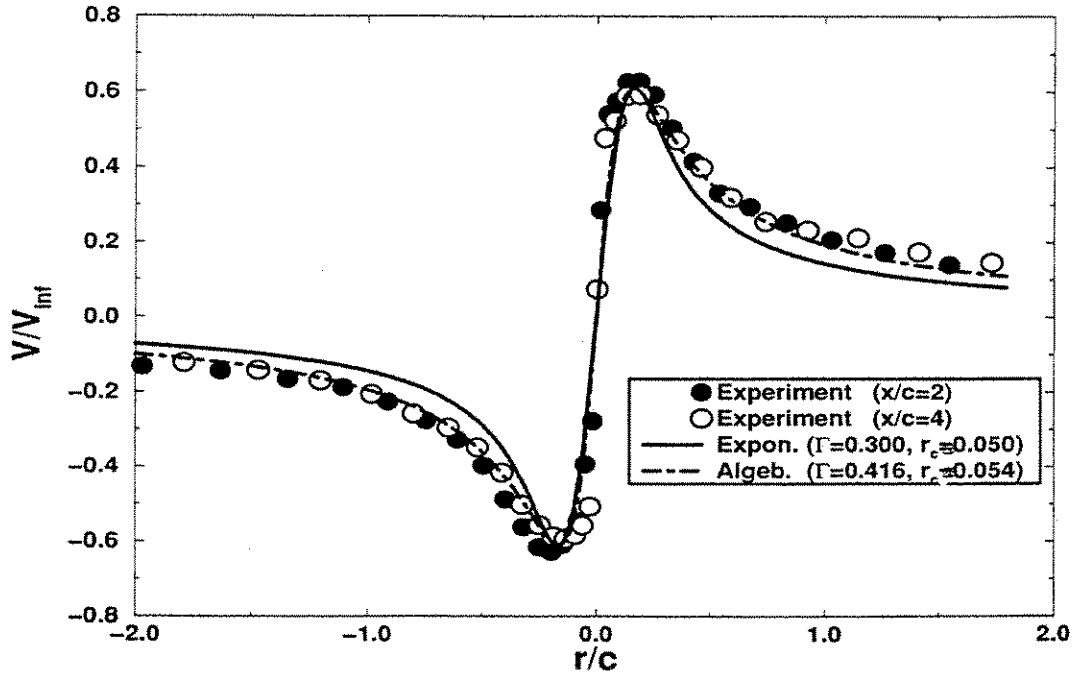

Figures 8. Comparison of two modified vortex models to the McAlister data.

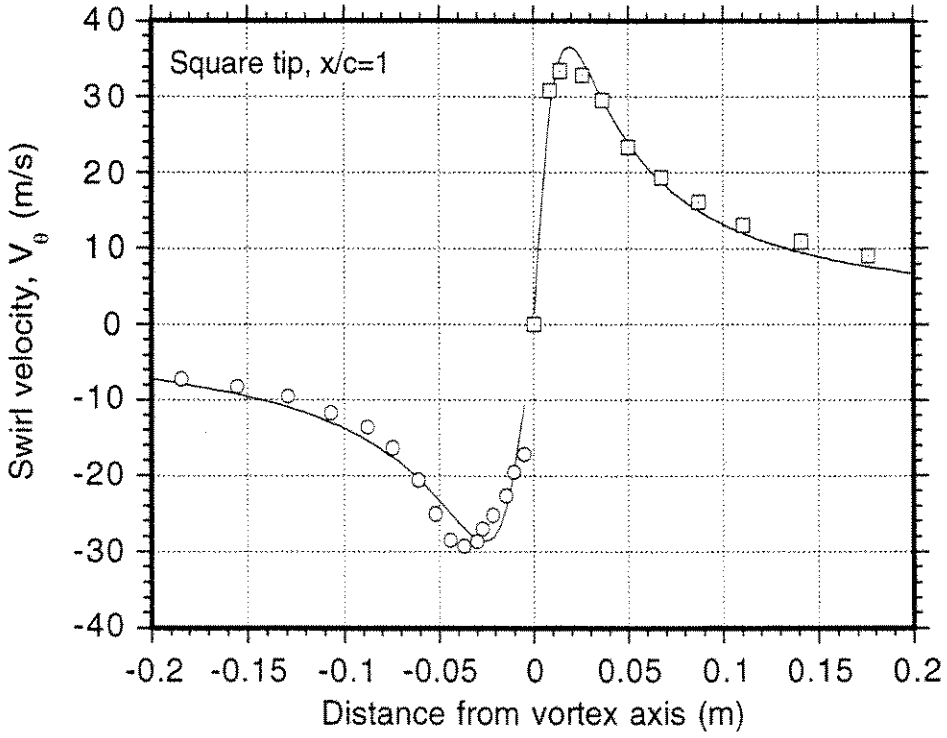

Figure 9. Vortex characteristics 2 chords downstream of VG trailing edge.

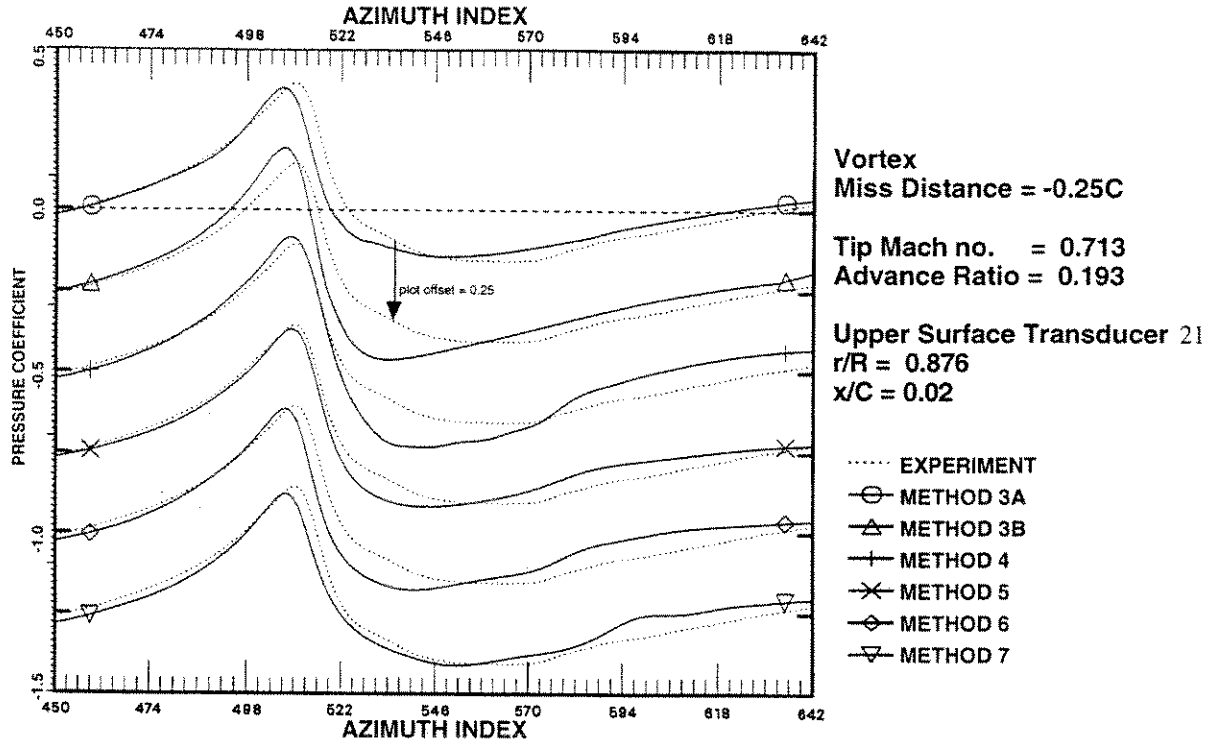

Figure 10a. A comparison of computational methods with experimental data for Case 1D, Upper Blade Surface, Transducer 21.

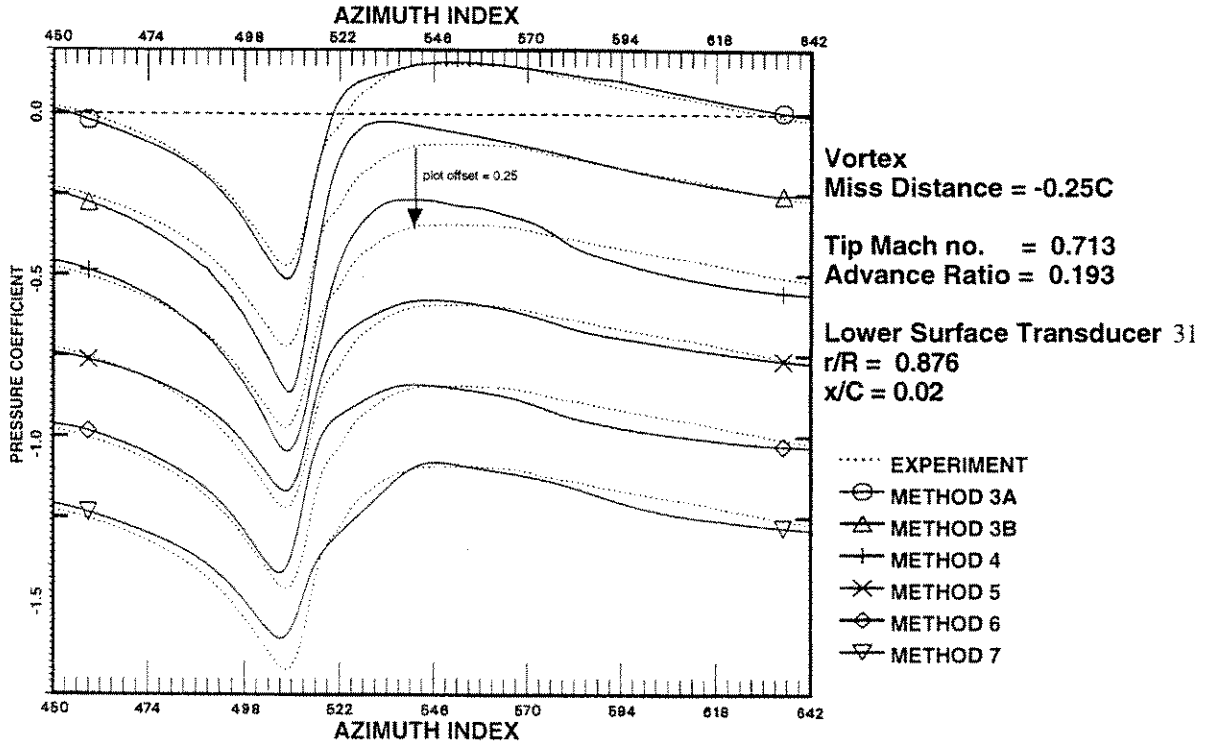

Figure 10b. A comparison of computational methods with experimental data for Case 1D, Lower Blade Surface, Transducer 31.

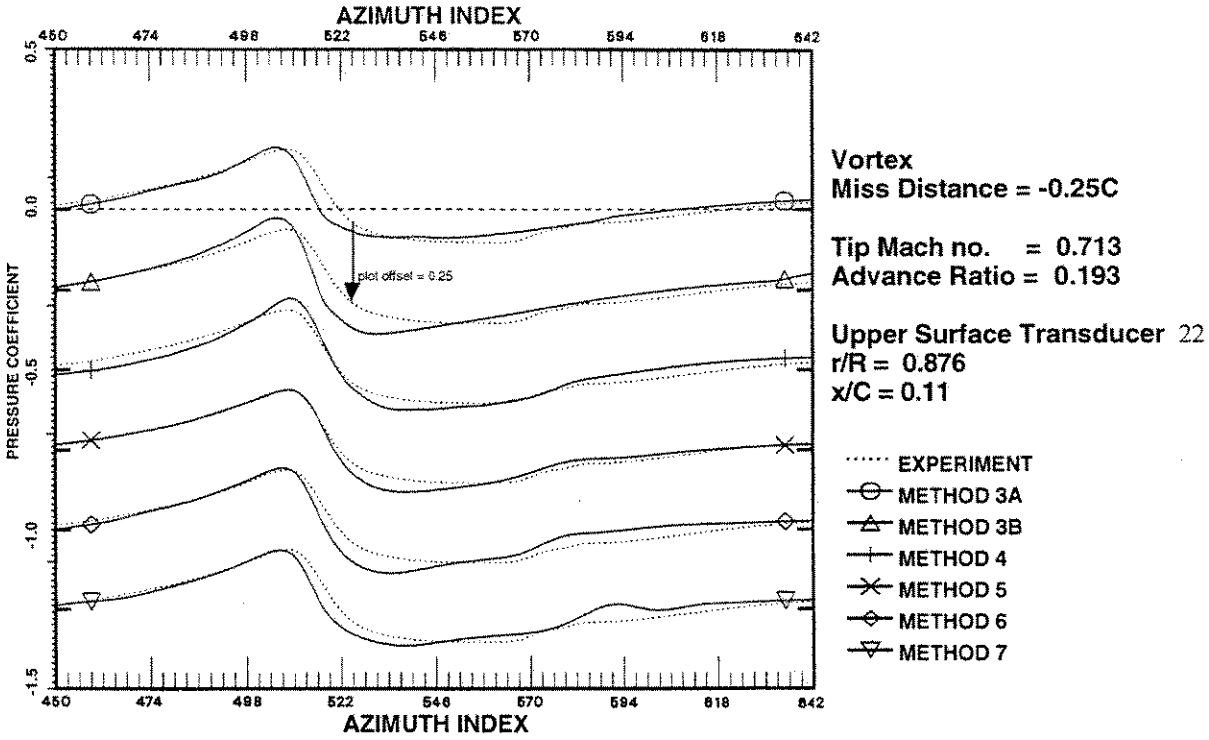

Figure 11a. A comparison of computational methods with experimental data for Case 1D, Upper Blade Surface, Transducer 22.

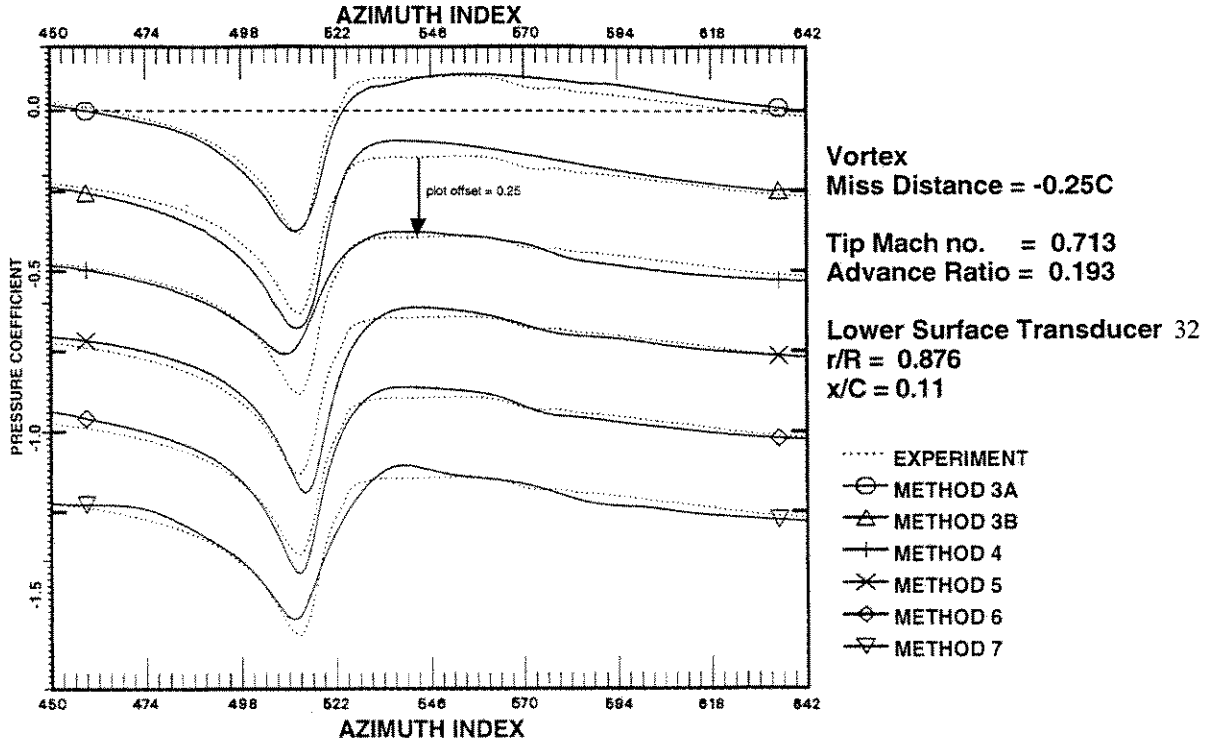

Figure 11b. A comparison of computational methods with experimental data for Case 1D, Lower Blade Surface, Transducer 32.

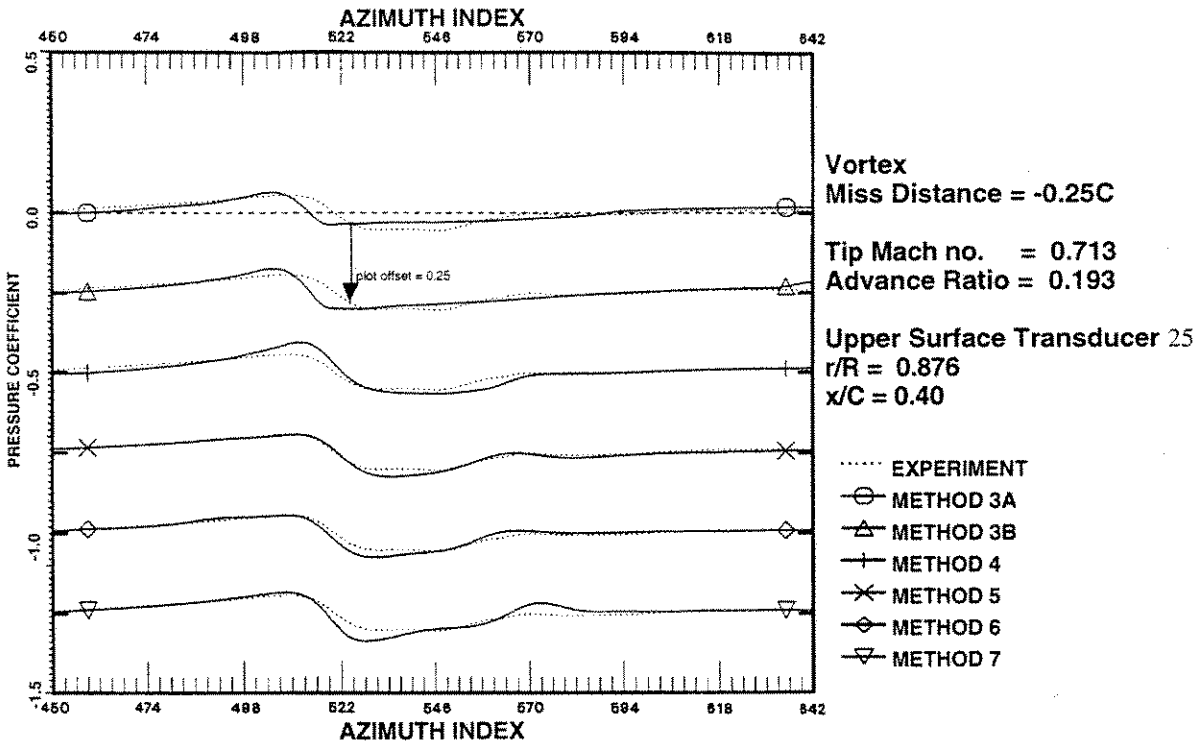

Figure 12a. A comparison of computational methods with experimental data for Case 1D, Upper Blade Surface, Transducer 25.

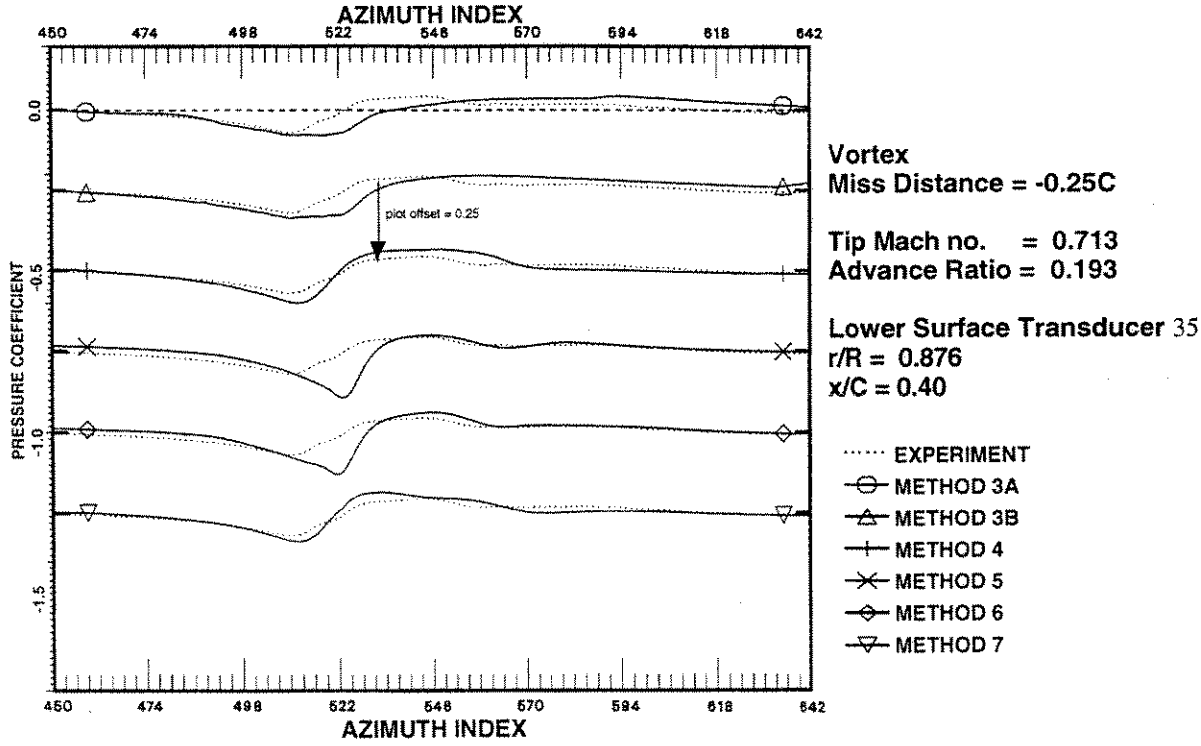

Figure 12b. A comparison of computational methods with experimental data for Case 1D, Lower Blade Surface, Transducer 35.

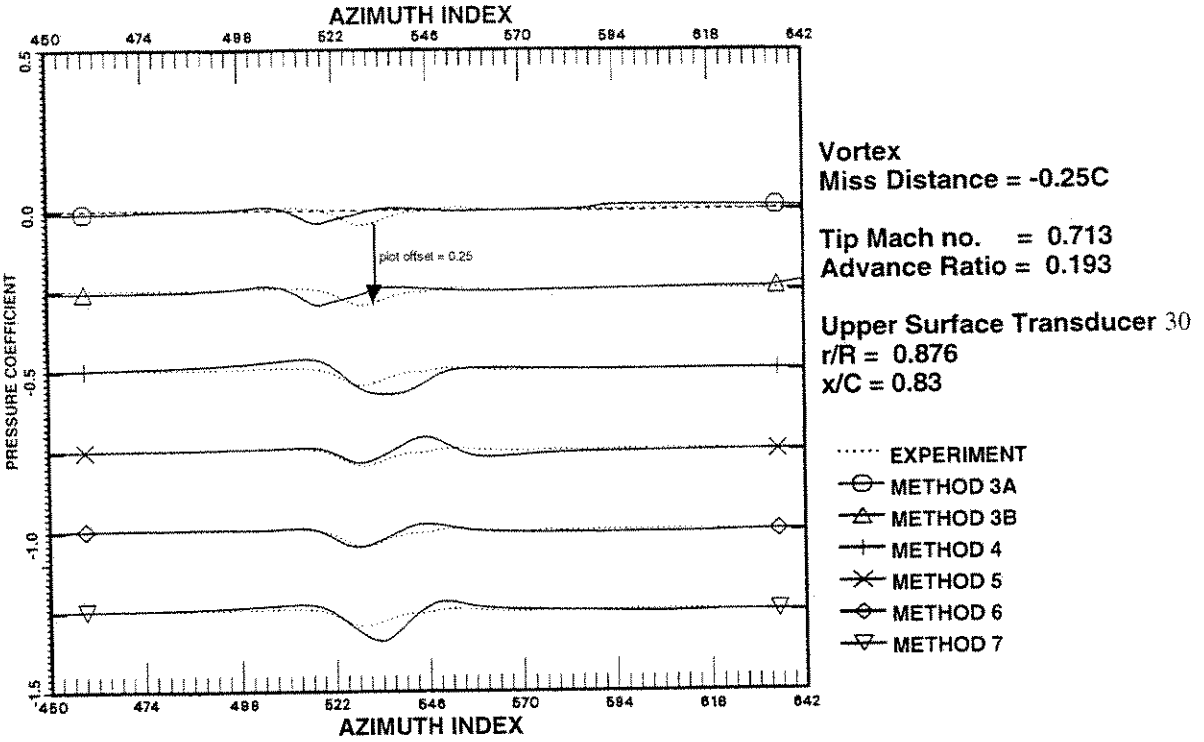

Figure 13a. A comparison of computational methods with experimental data for Case 1D, Upper Blade Surface, Transducer 30.

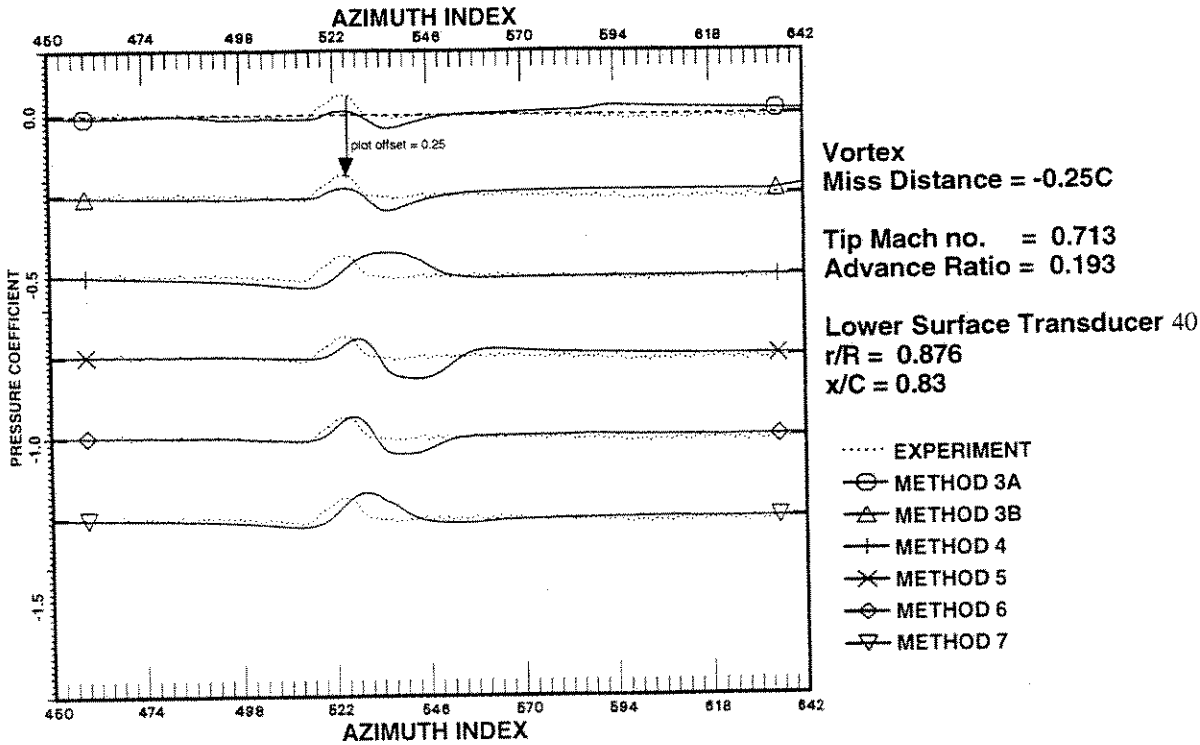

Figure 13b. A comparison of computational methods with experimental data for Case 1D, Lower Blade Surface, Transducer 40.

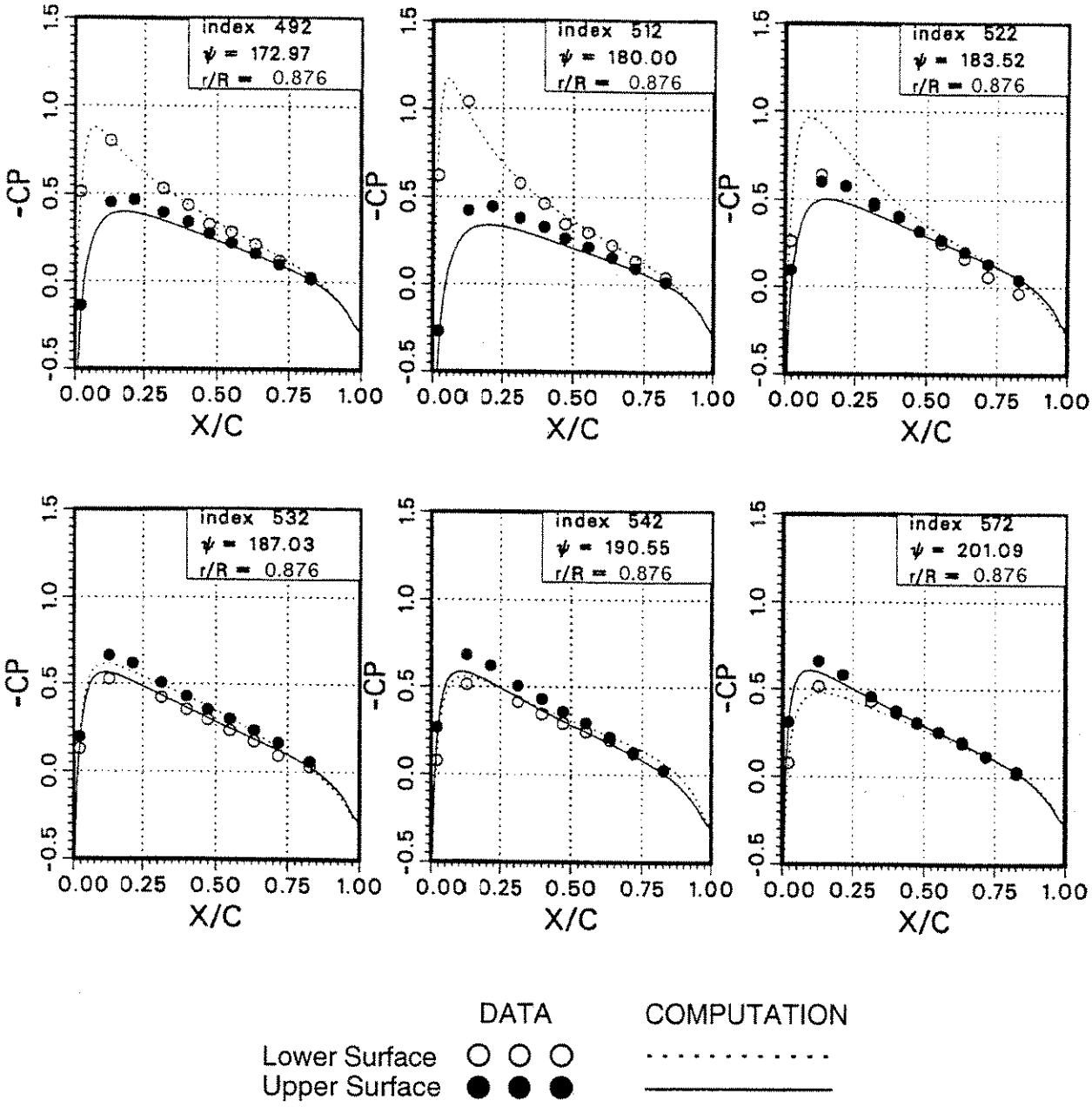

Figure 14. A comparison of computation with BVI data for Case 1D computed using Method 3A.

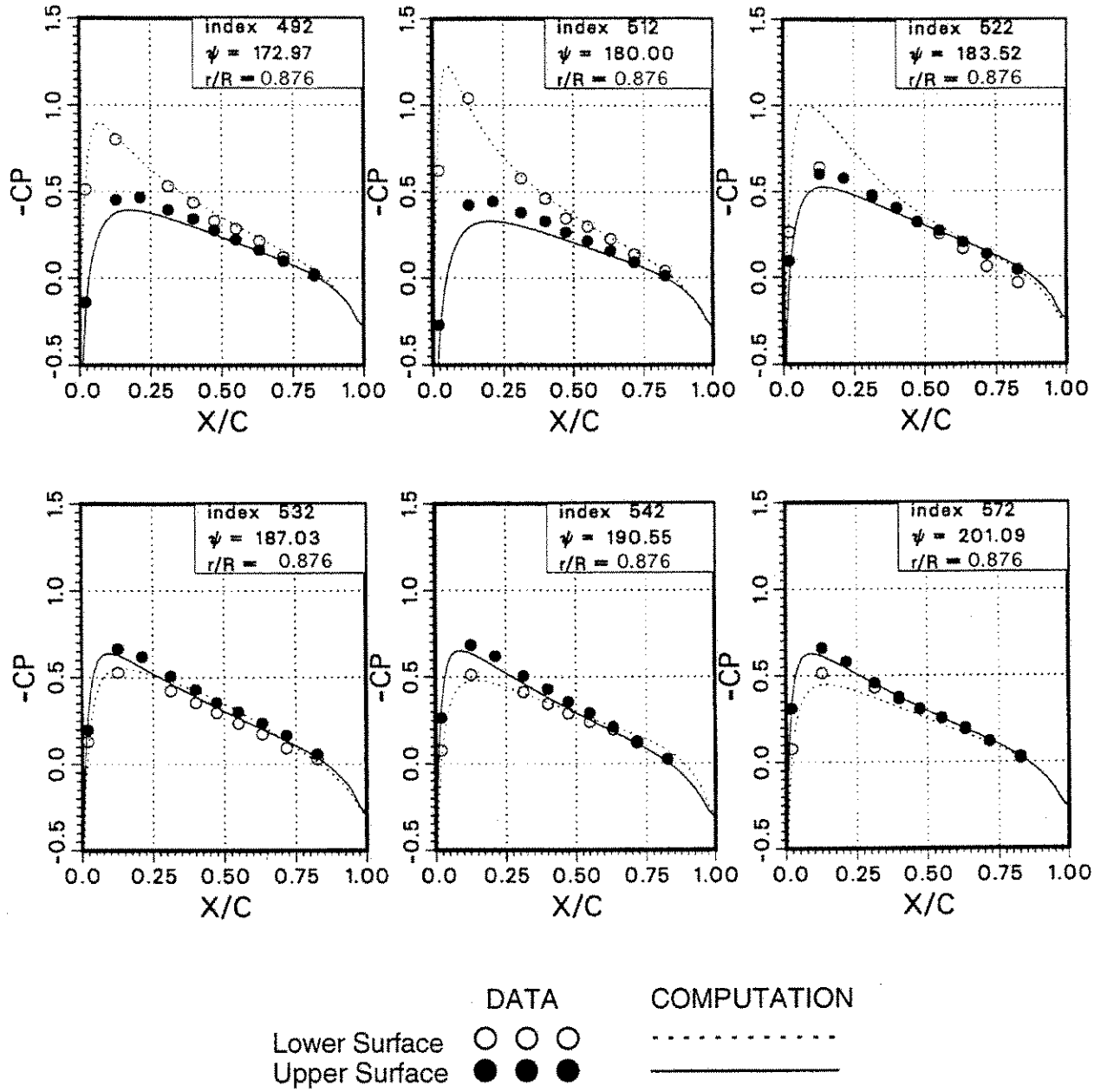

Figure 15. A comparison of computation with BVI data for Case 1D computed using Method 3B.

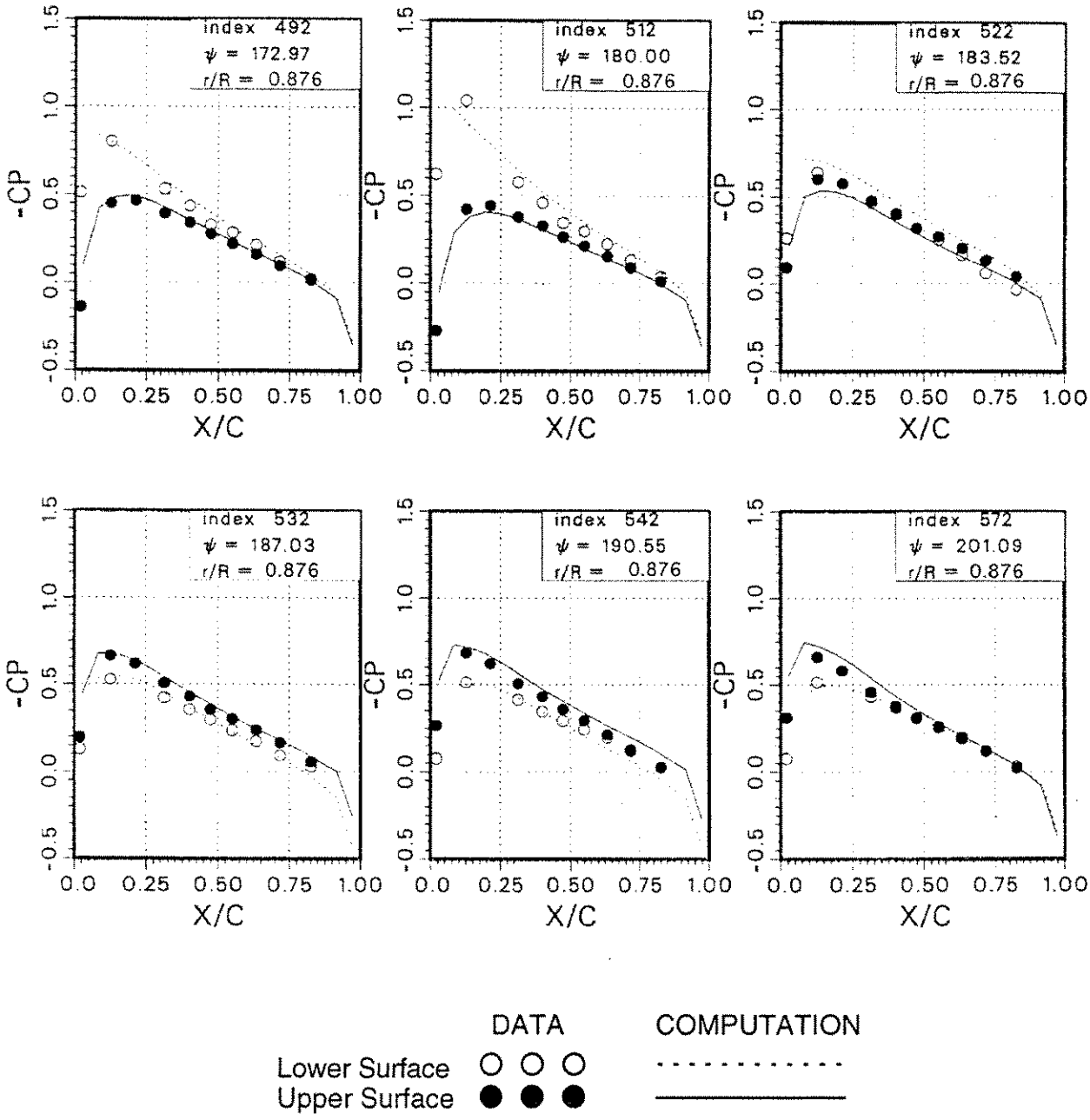

Figure 16. A comparison of computation with BVI data for Case 1D computed using Method 4.

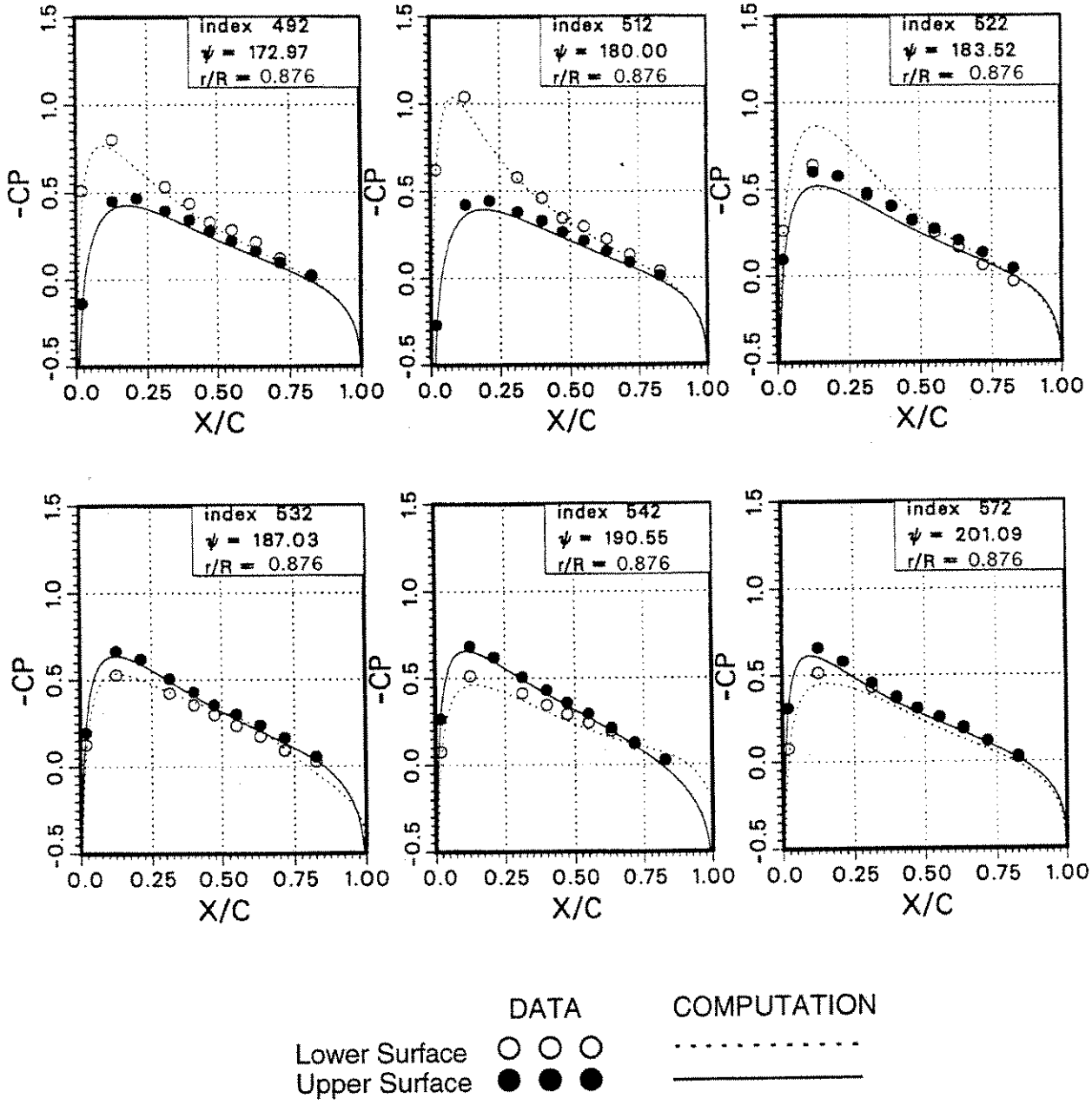

Figure 17. A comparison of computation with BVI data for Case 1D computed using Method 5.

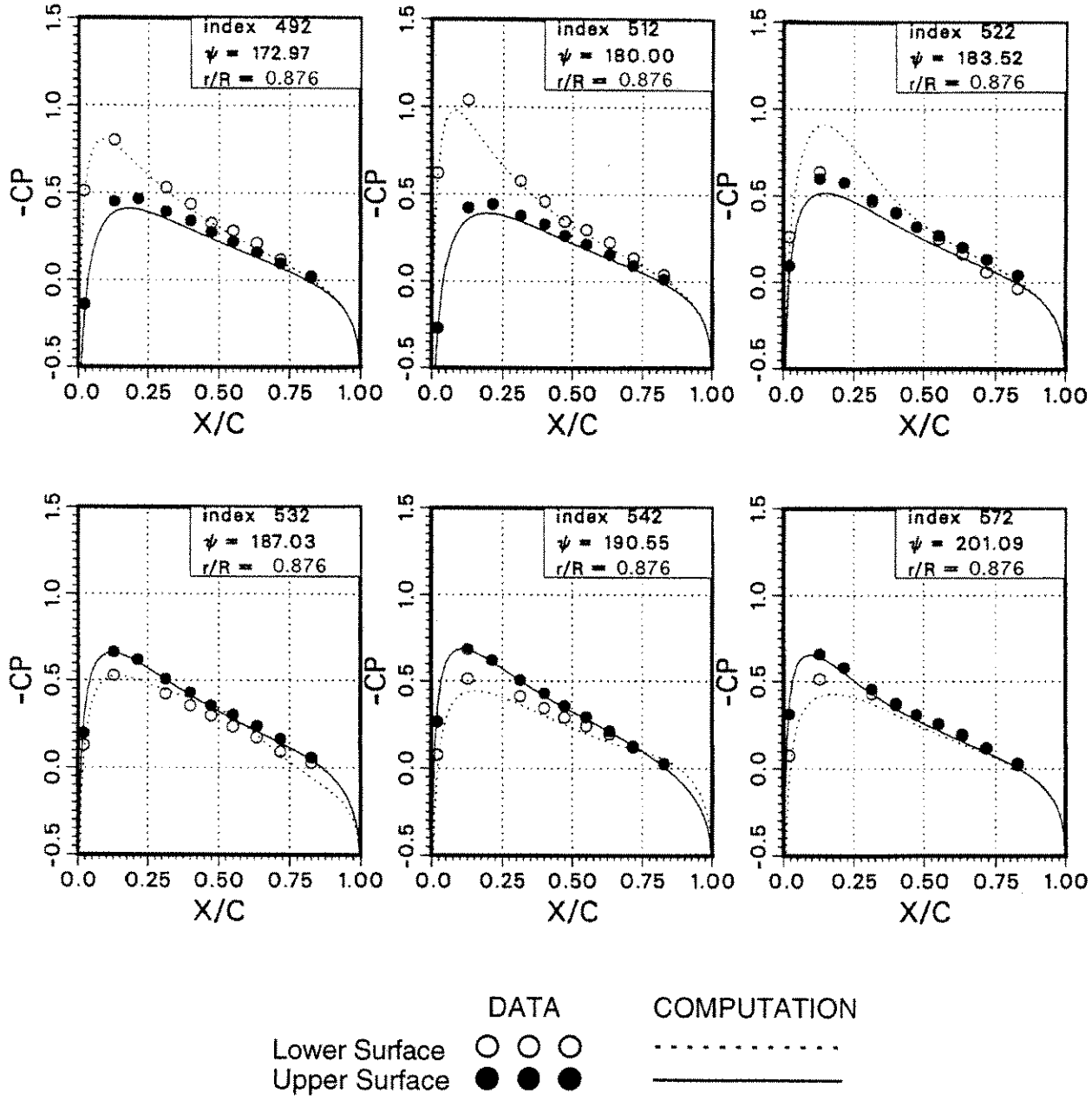

Figure 18. A comparison of computation with BVI data for Case 1D computed using Method 6.

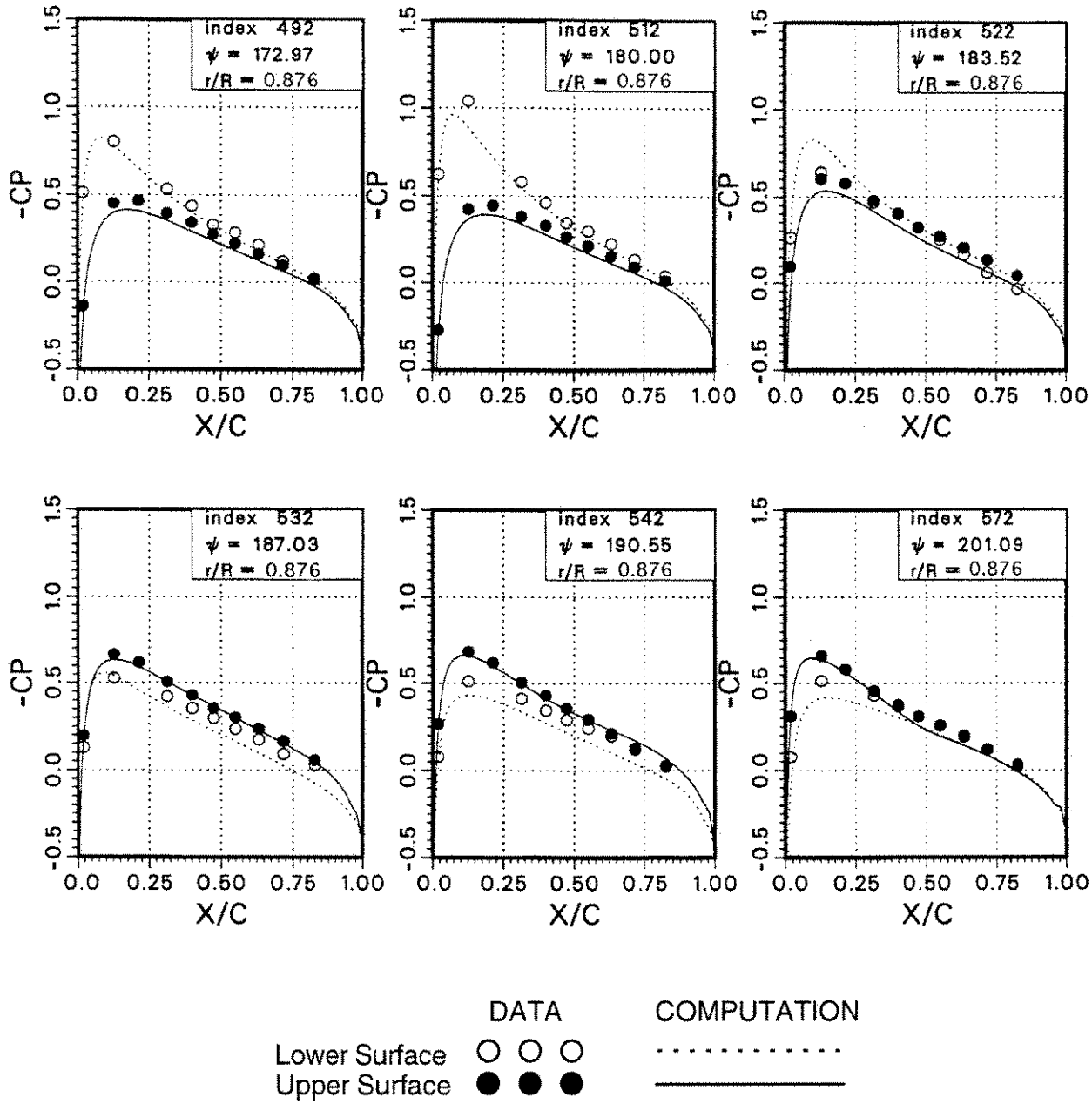

Figure 19. A comparison of computation with BVI data for Case 1D computed using Method 7.

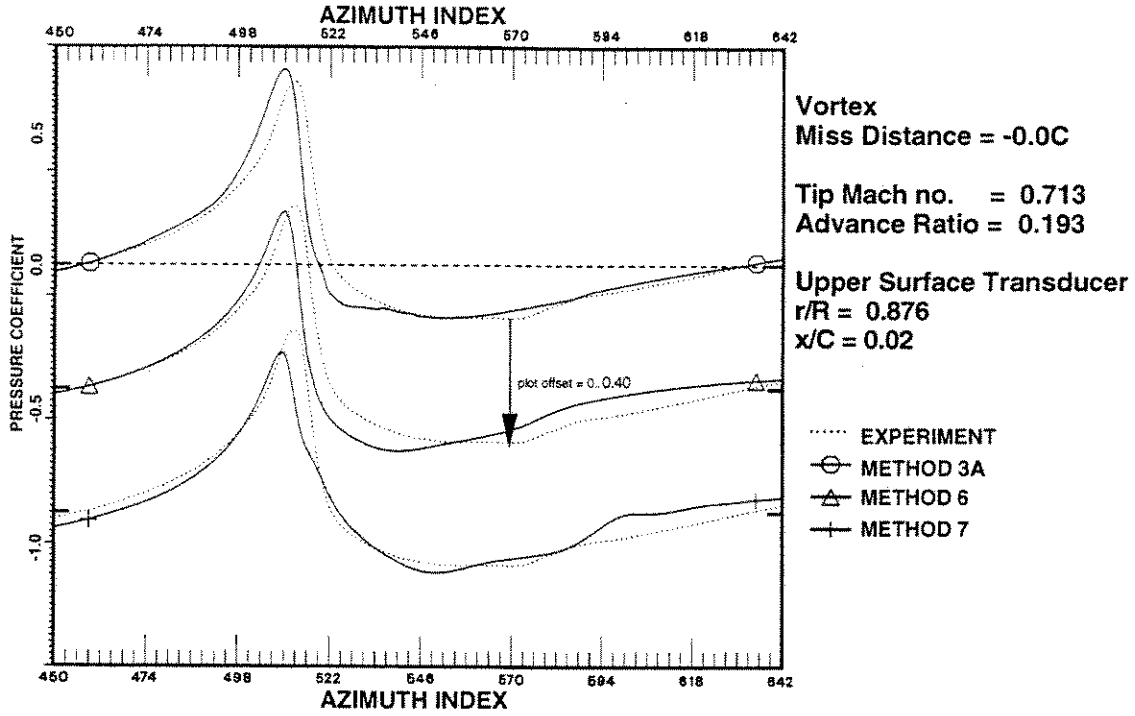

Figure 20a. A comparison of computational methods with experimental data for Case 1B, Upper Blade Surface, Transducer 21.

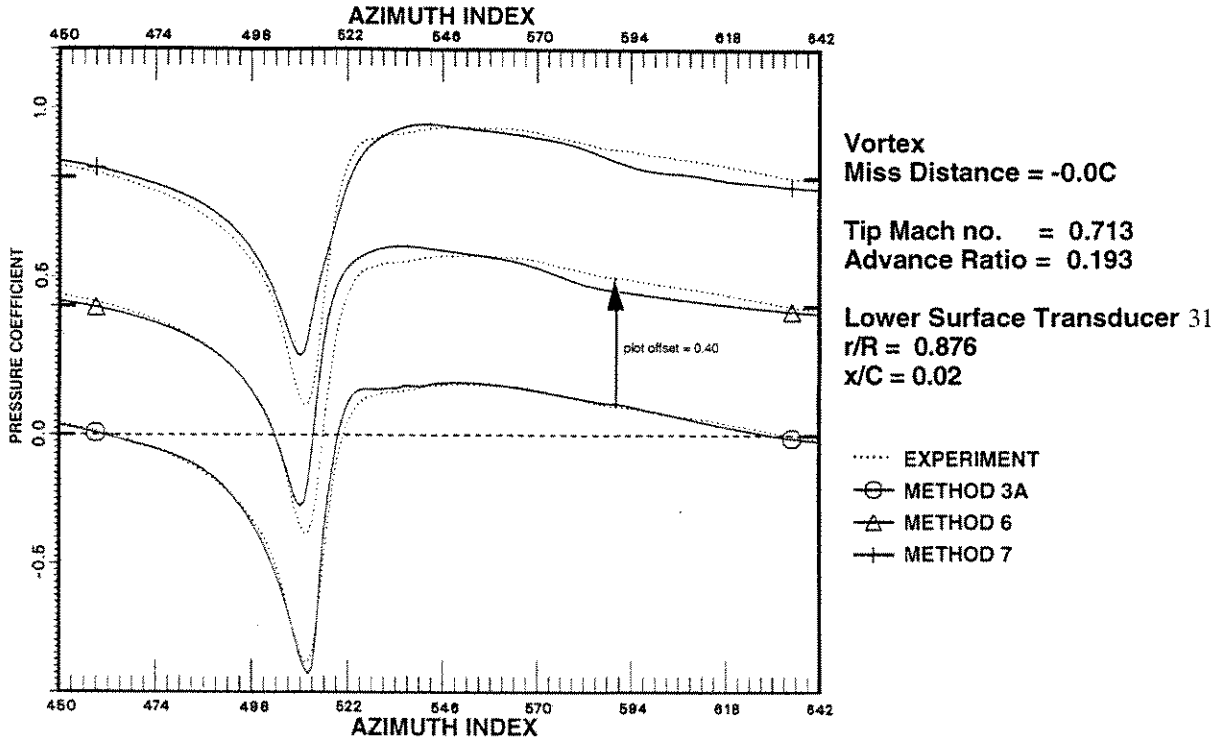

Figure 20b: A comparison of computational methods with experimental data for Case 1B, Lower Blade Surface, Transducer 31.

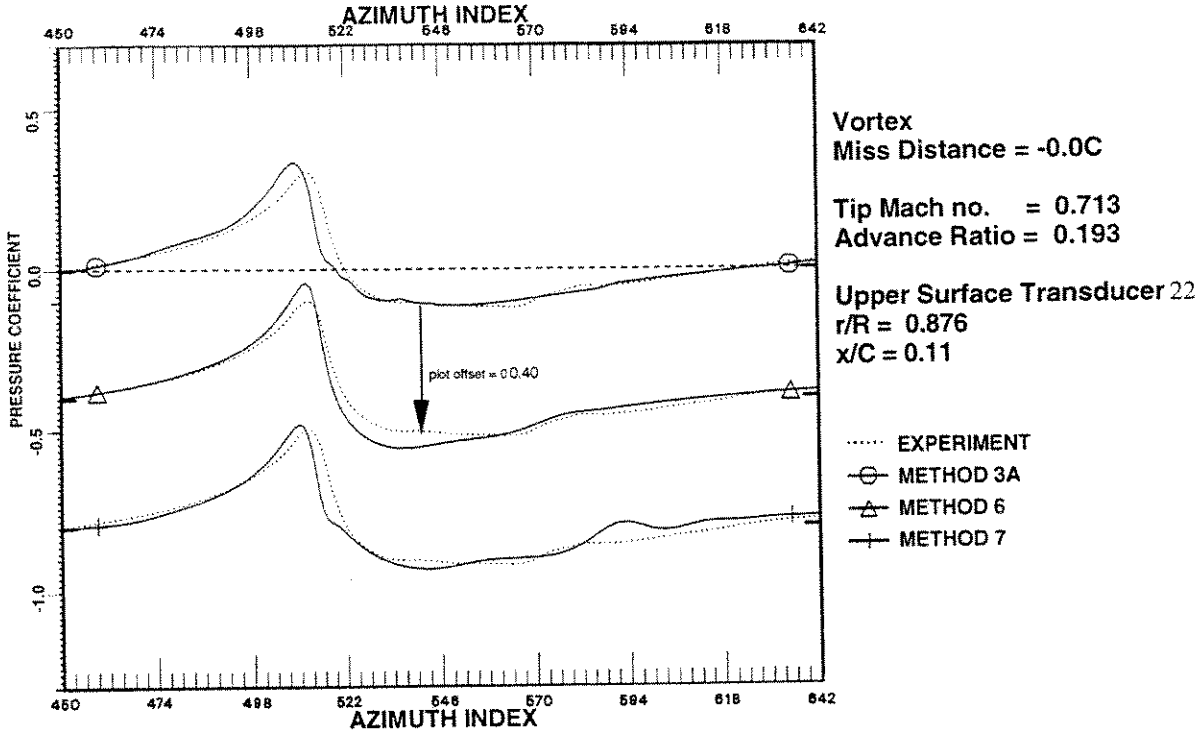

Figure 21a. A comparison of computational methods with experimental data for Case 1B, Upper Blade Surface, Transducer 22.

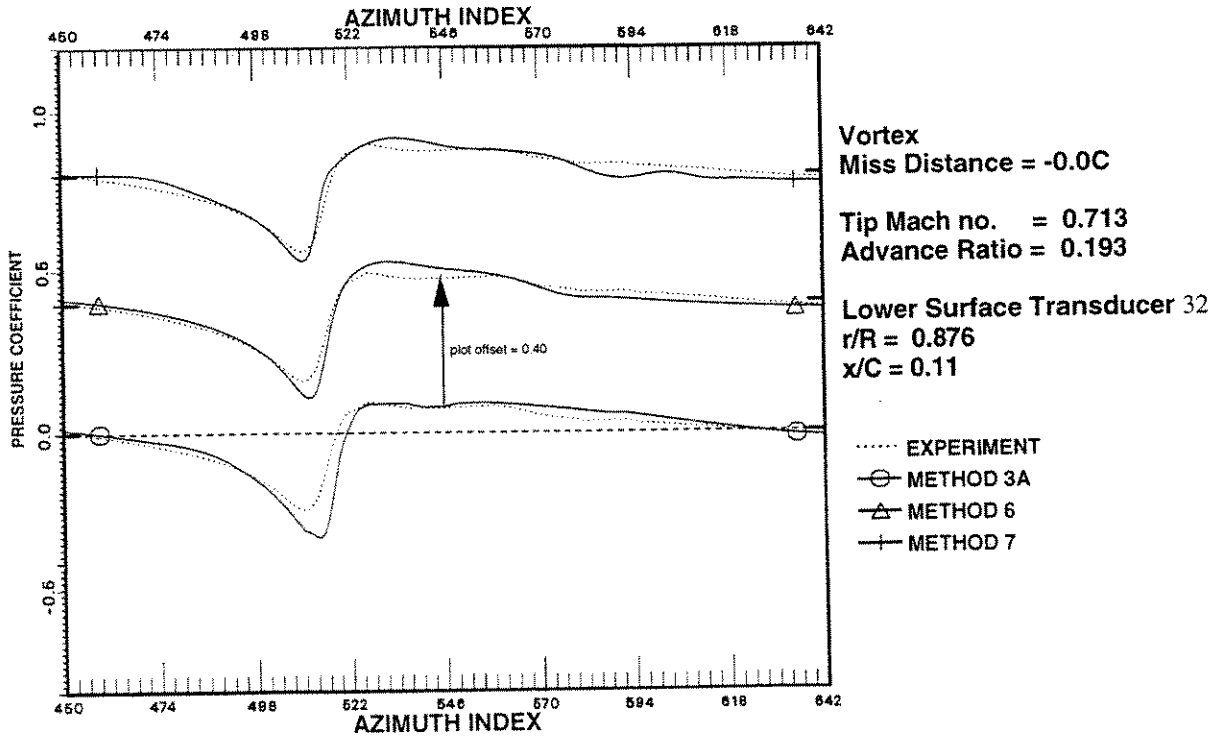

Figure 21b. A comparison of computational methods with experimental data for Case 1B, Lower Blade Surface, Transducer 32.

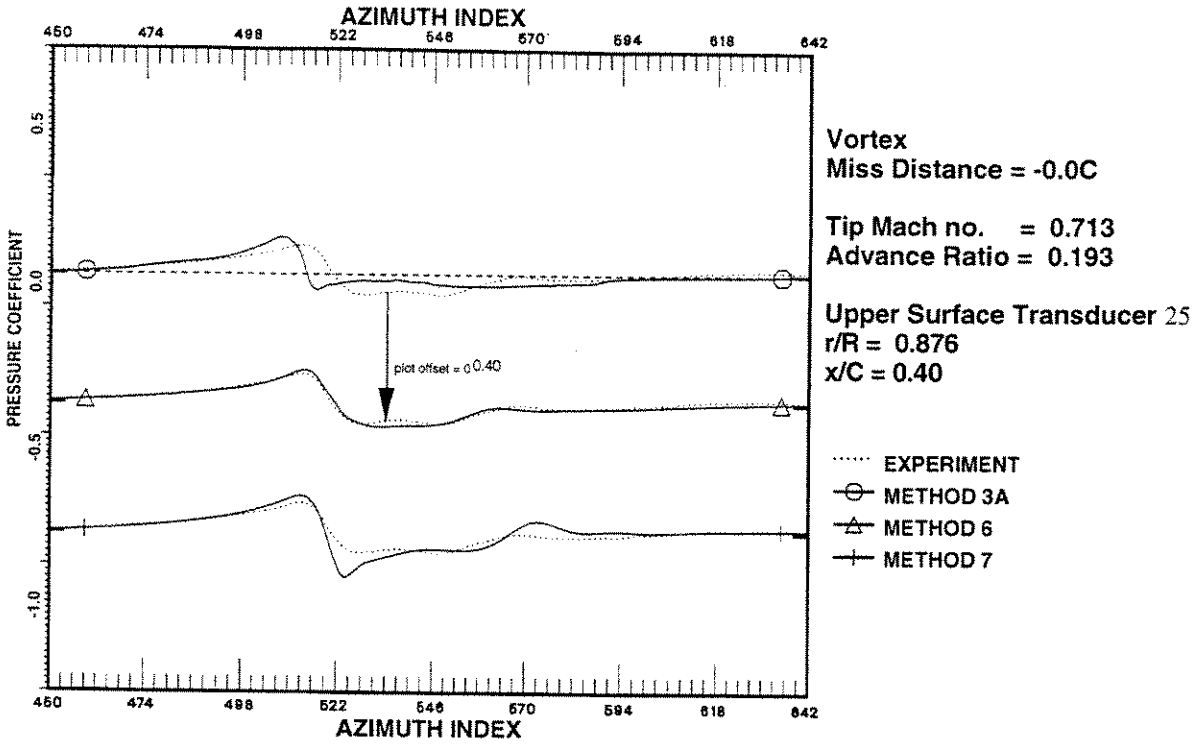

Figure 22a. A comparison of computational methods with experimental data for Case 1B, Upper Blade Surface, Transducer 25.

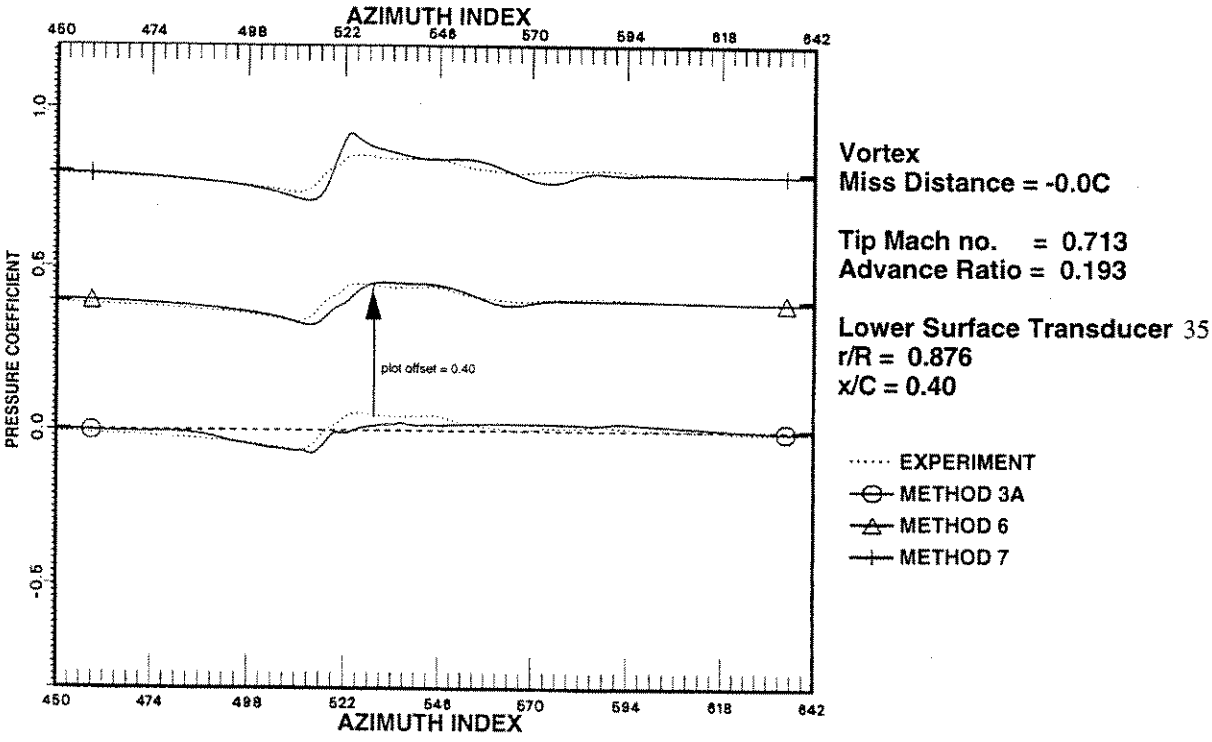

Figure 22b. A comparison of computational methods with experimental data for Case 1B, Lower Blade Surface, Transducer 35.

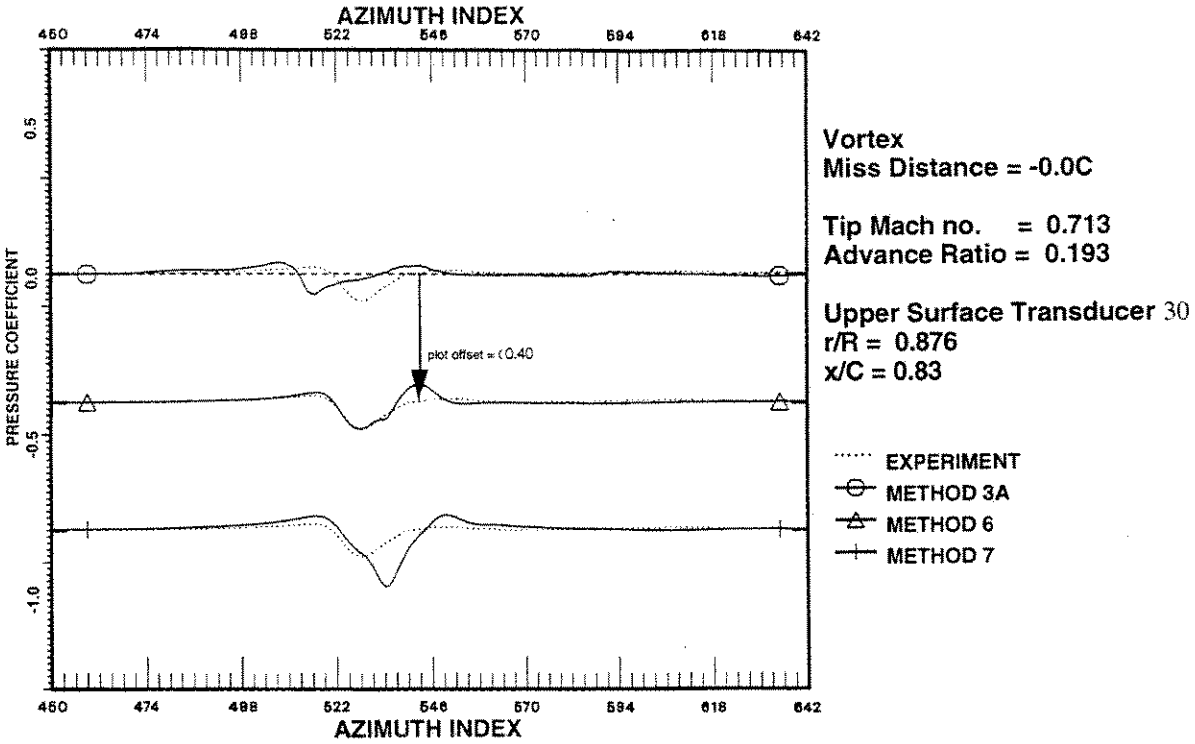

Figure 23a. A comparison of computational methods with experimental data for Case 1B, Upper Blade Surface, Transducer 30.

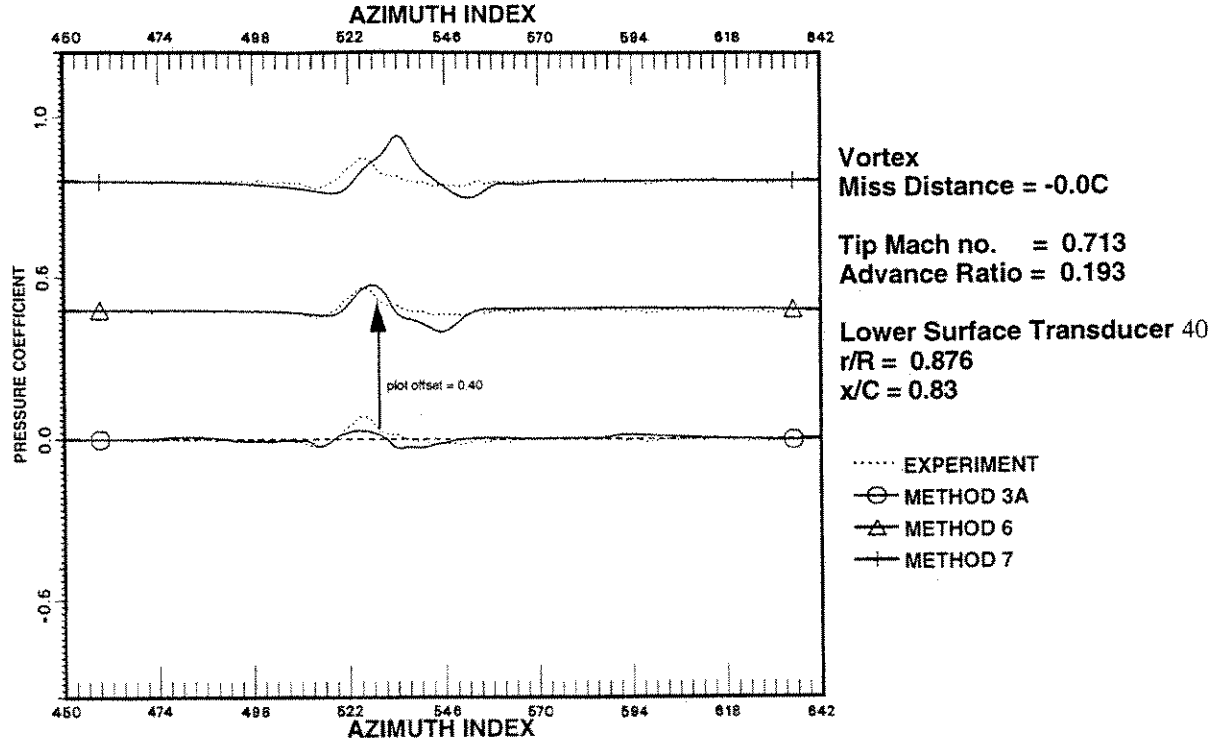

Figure 23b. A comparison of computational methods with experimental data for Case 1B, Lower Blade Surface, Transducer 40.

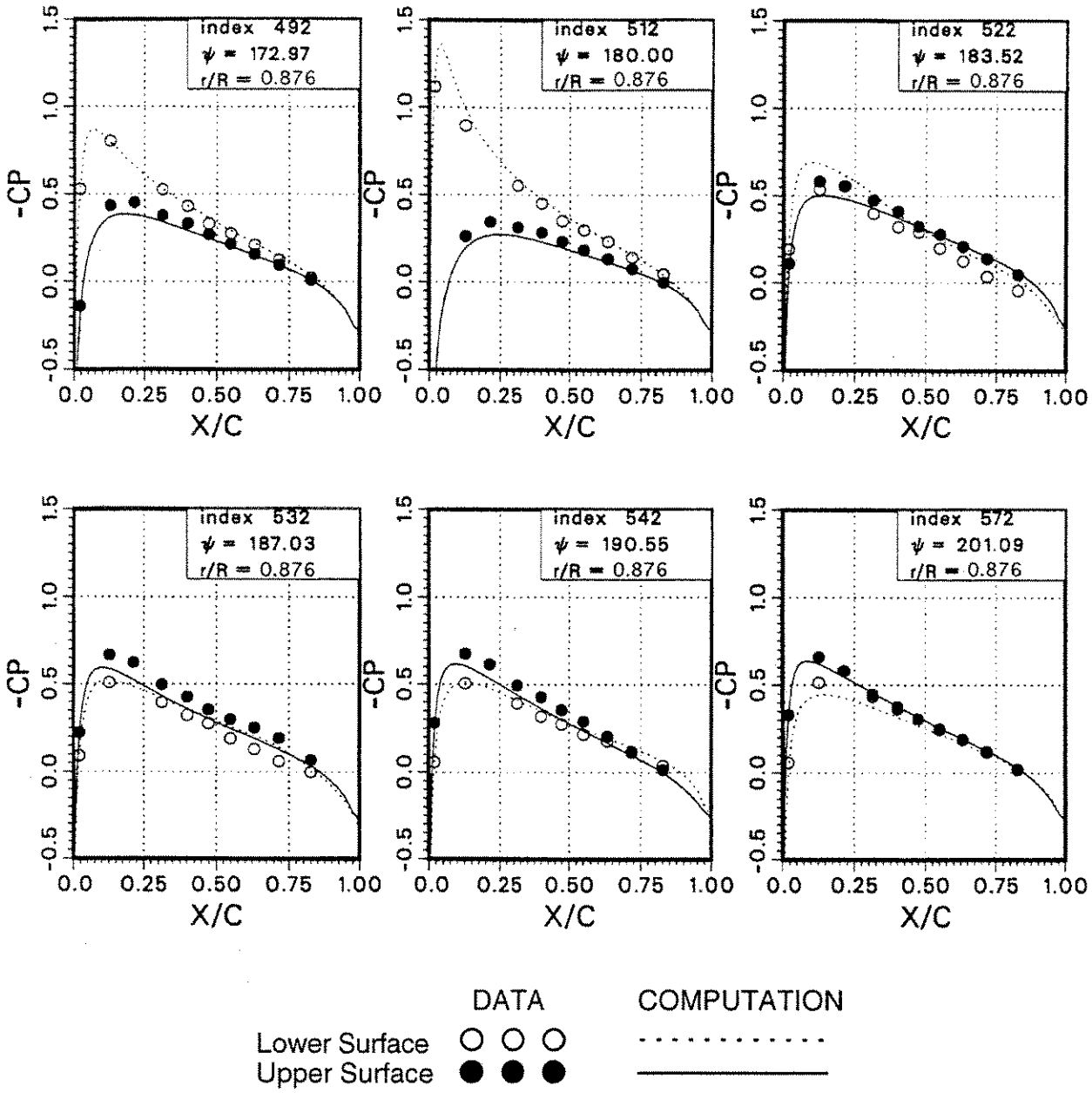

Figure 24. A comparison of computation with BVI data for Case 1B computed using Method 3A.

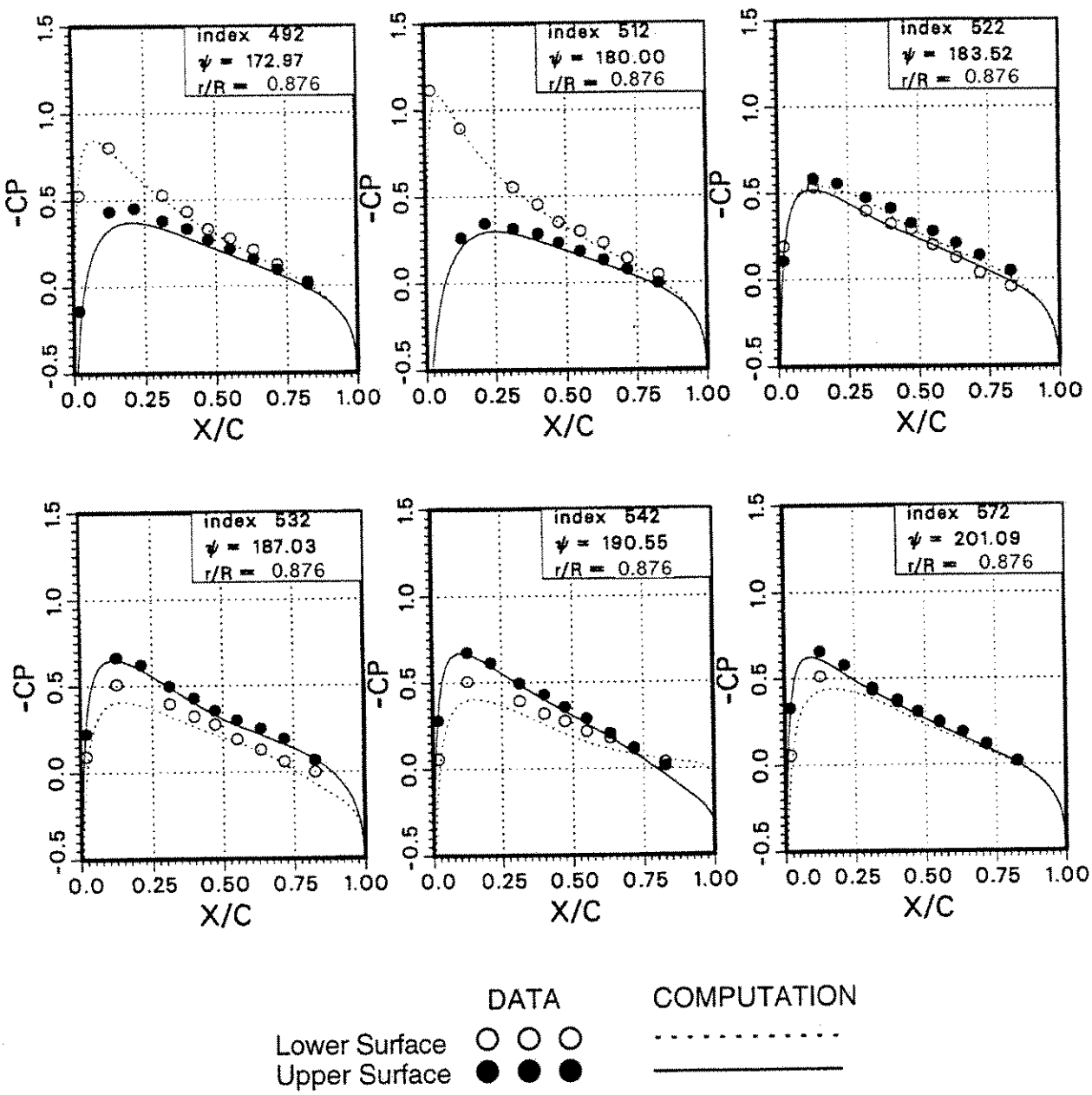

Figure 25. A comparison of computation with BVI data for Case 1B computed using Method 6.

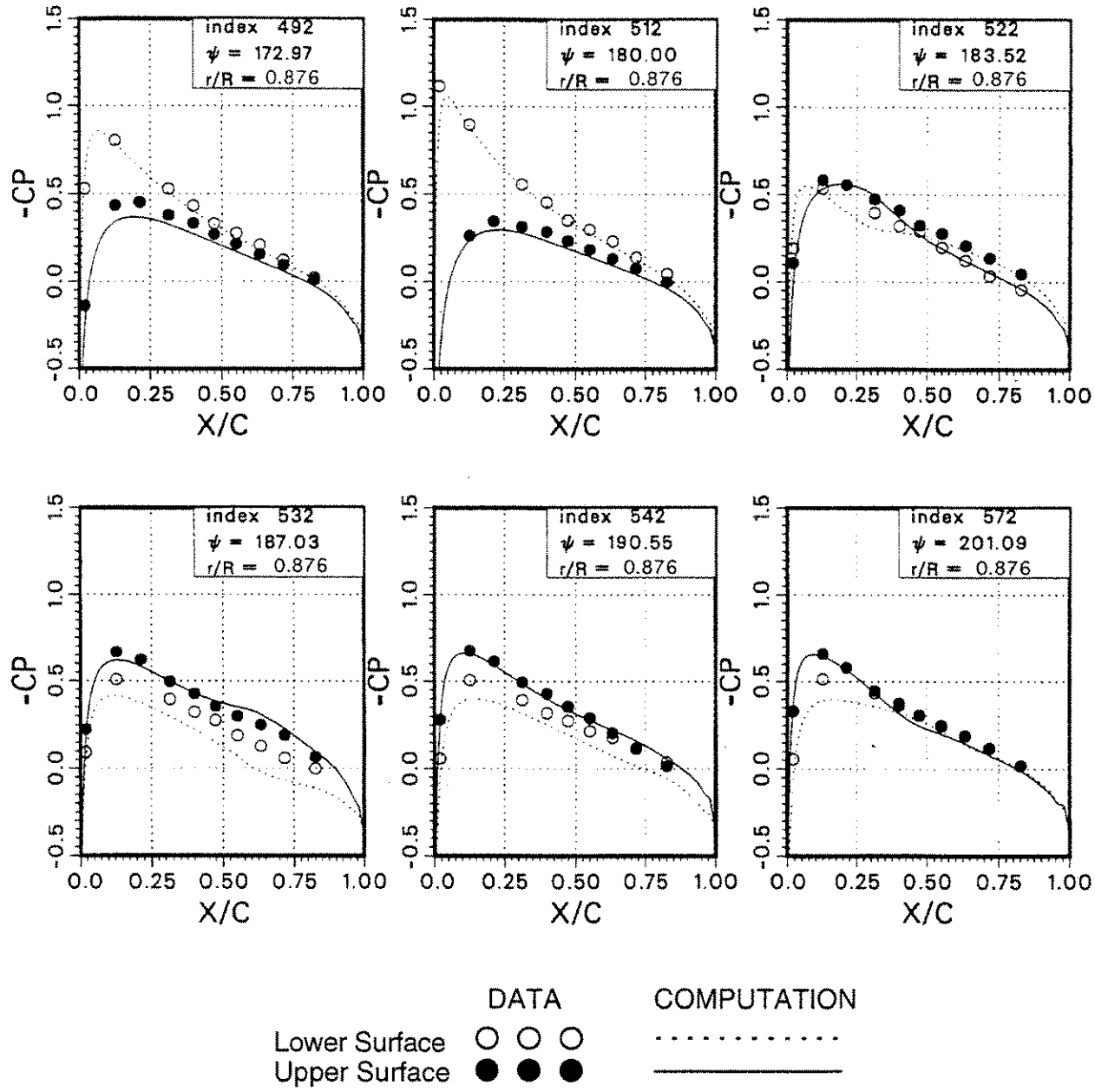

Figure 26. A comparison of computation with BVI data for Case 1B computed using Method7.

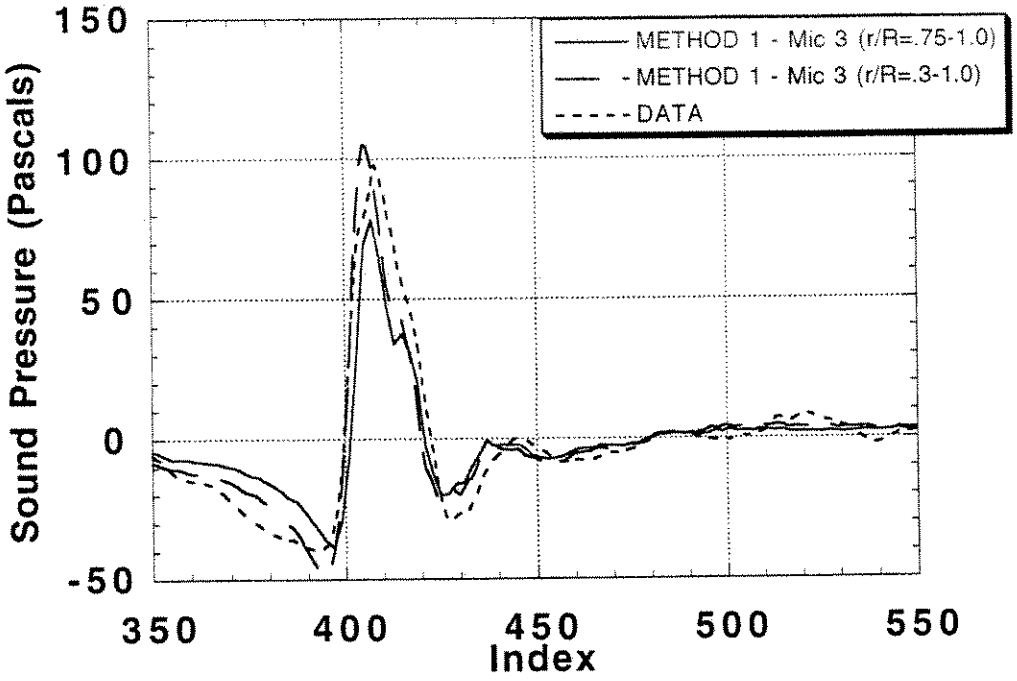

Figure 27a. Comparison of Method 1 computational results with experimental data at Microphone 3 for Case 1D.

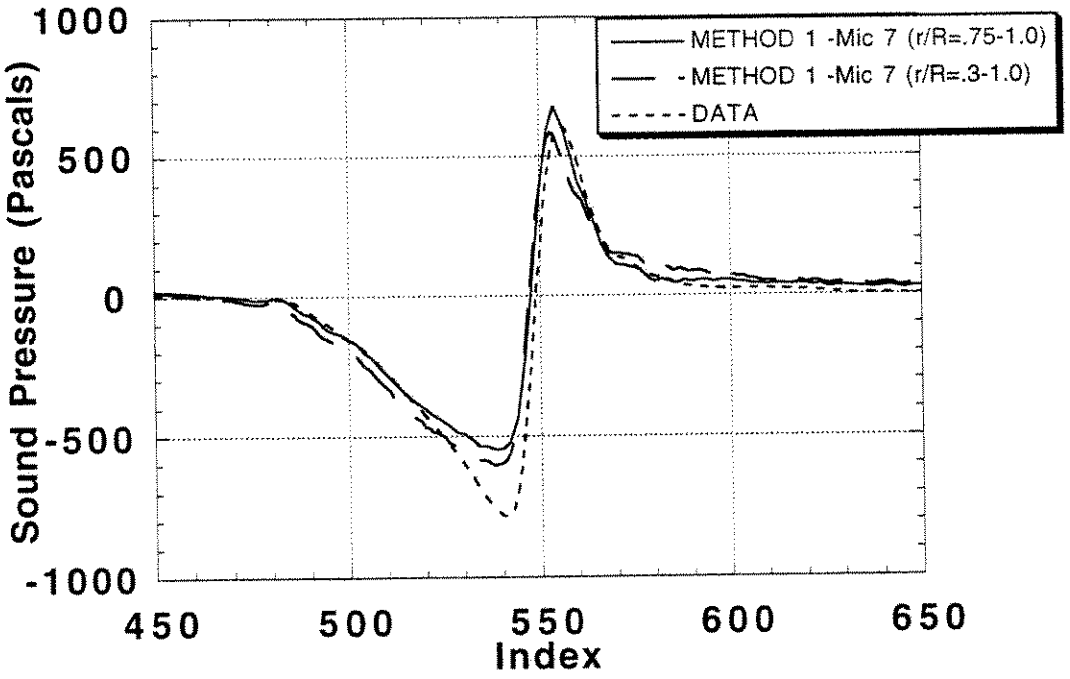

Figure 27b. Comparison of Method 1 computational results with experimental data at Microphone 7 for Case 1D.

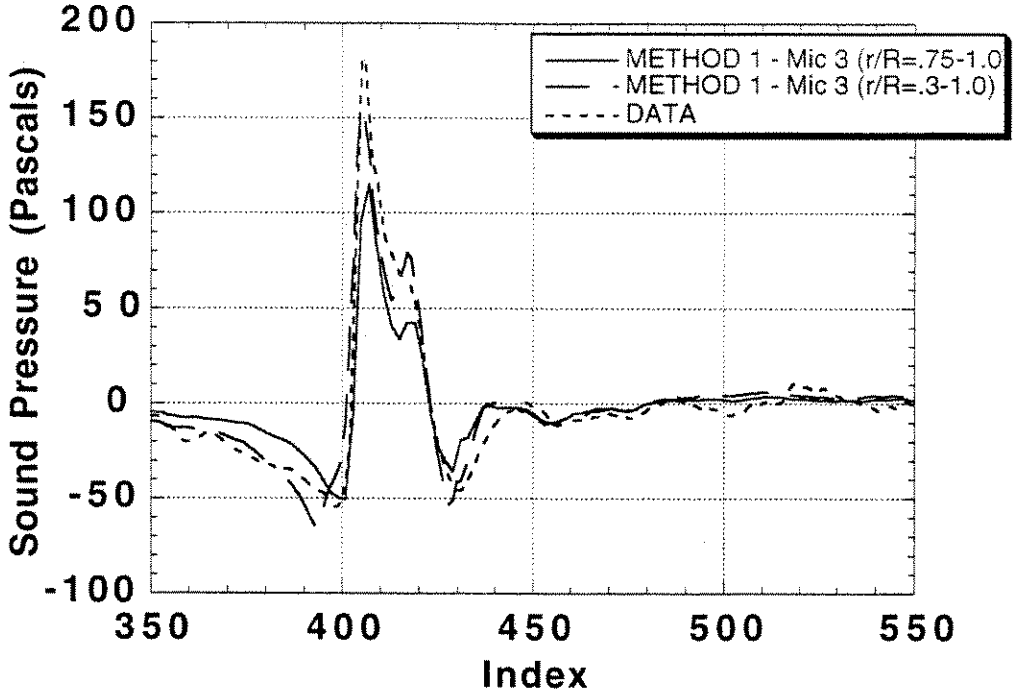

Figure 28a. Comparison of Method 1 computational results with experimental data at Microphone 3 for Case 1B.

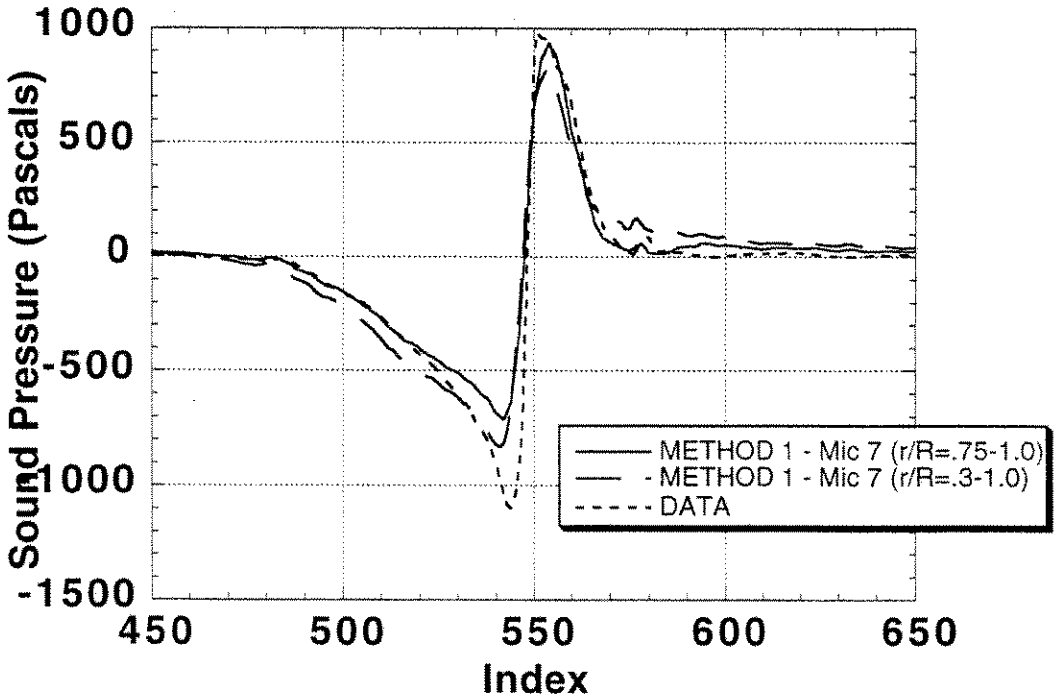

Figure 28b. Comparison of Method 1 computational results with experimental data at Microphone 7 for Case 1B.

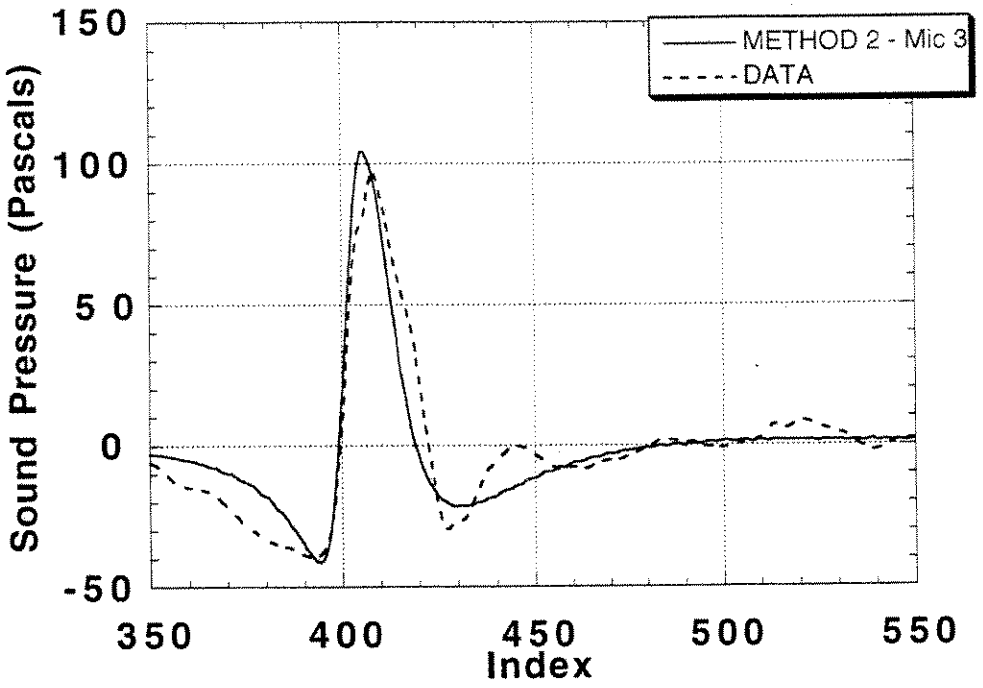

Figure 29a. Comparison of Method 2 computational results with experimental data at Microphone 3 for Case 1D.

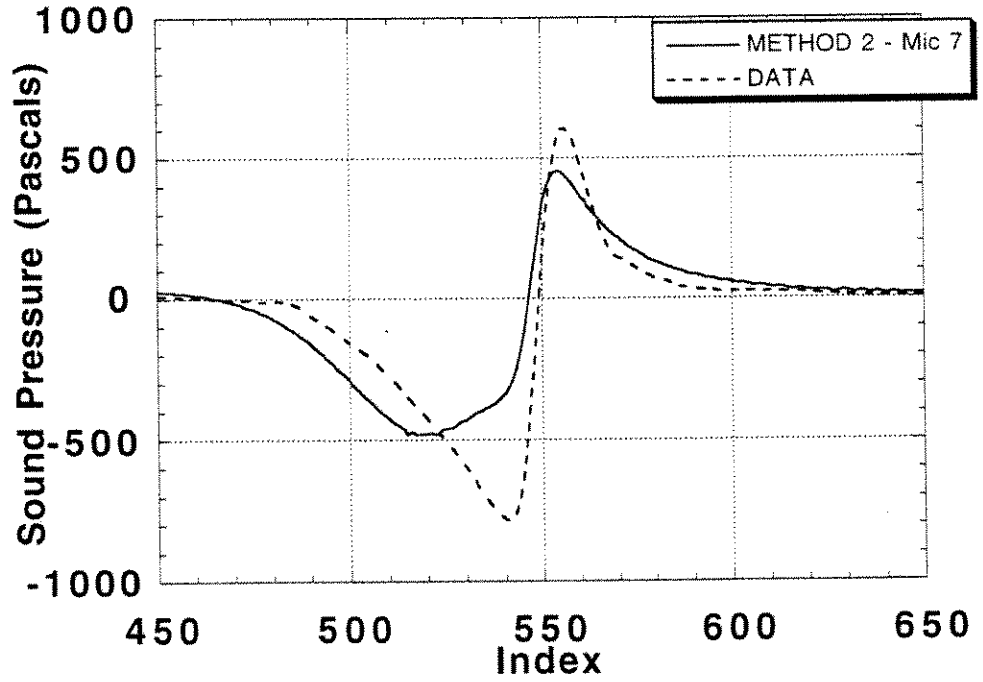

Figure 29b. Comparison of Method 2 computational results with experimental data at Microphone 7 for Case 1D.

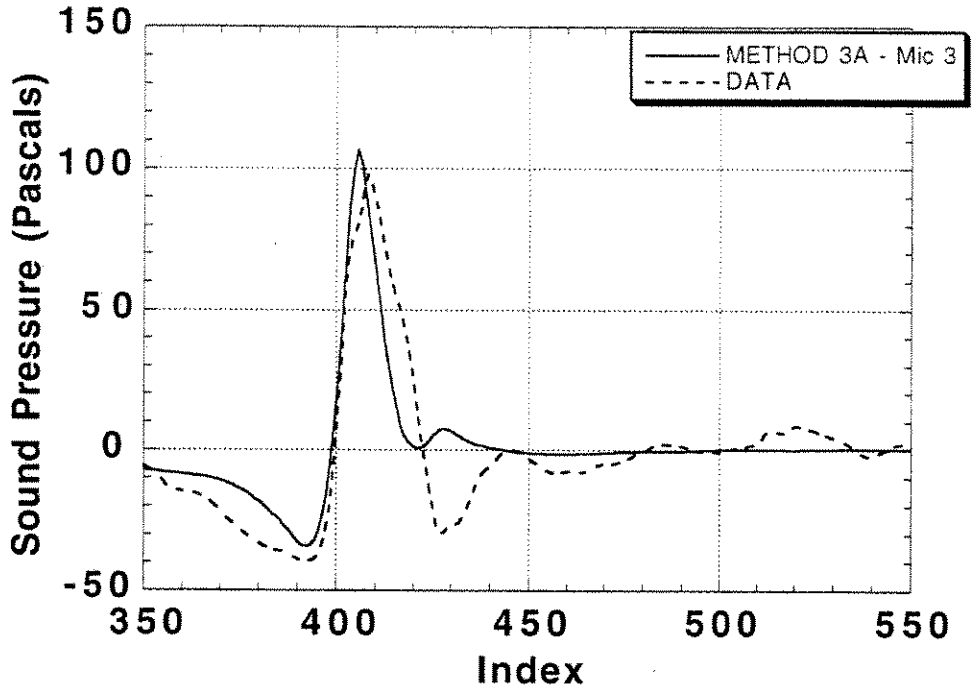

Figure 30a. Comparison of Method 3A computational results with experimental data at Microphone 3 for Case 1D.

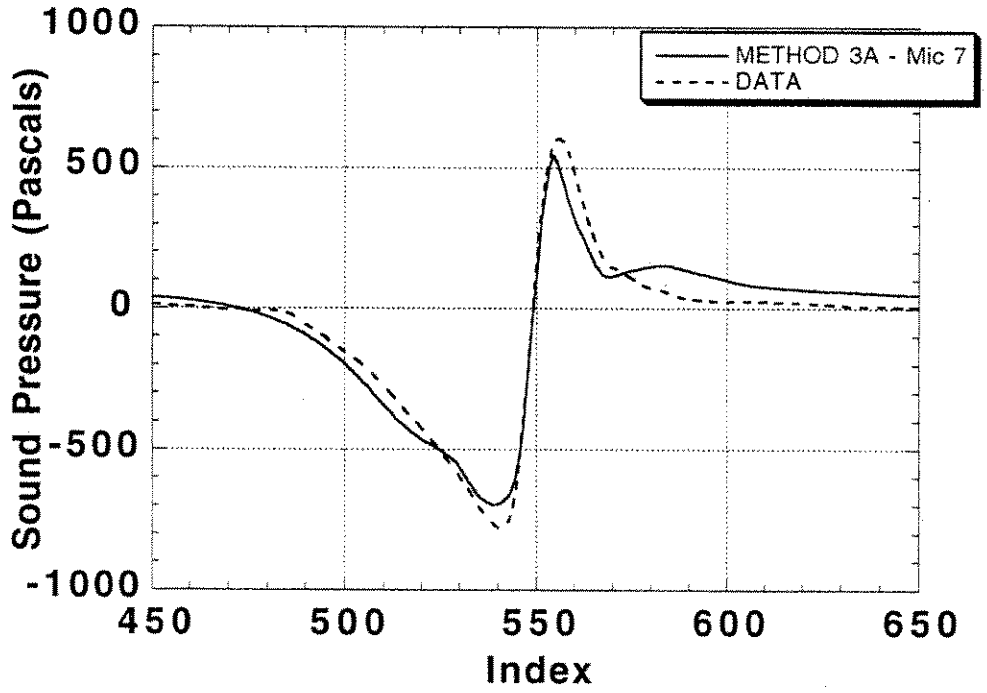

Figure 30b. Comparison of Method 3A computational results with experimental data at Microphone 7 for Case 1D.

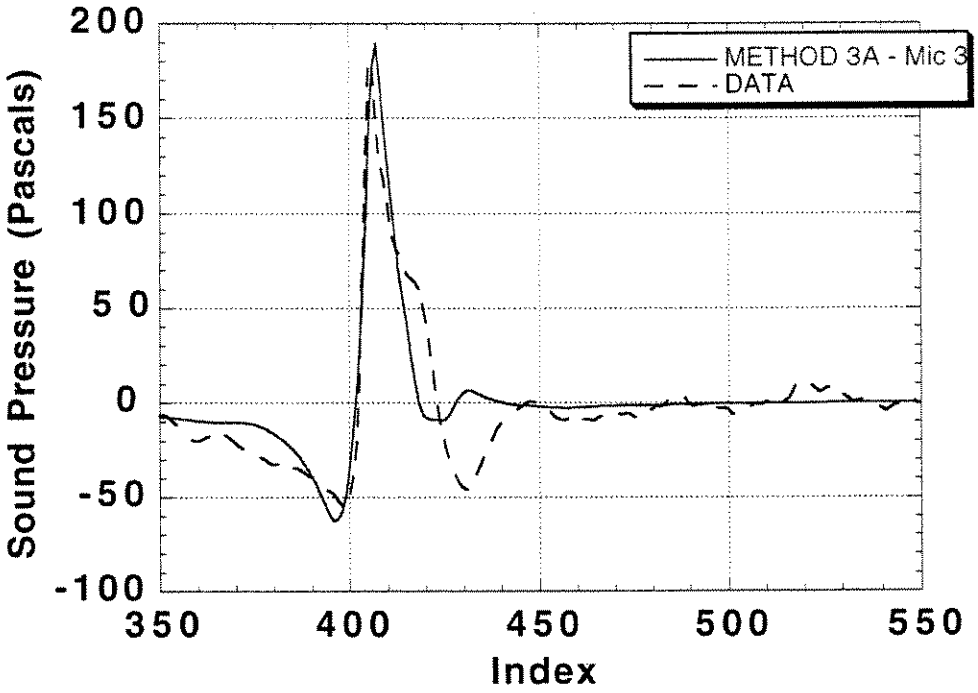

Figure 31a. Comparison of Method 3A computational results with experimental data at Microphone 3 for Case 1B.

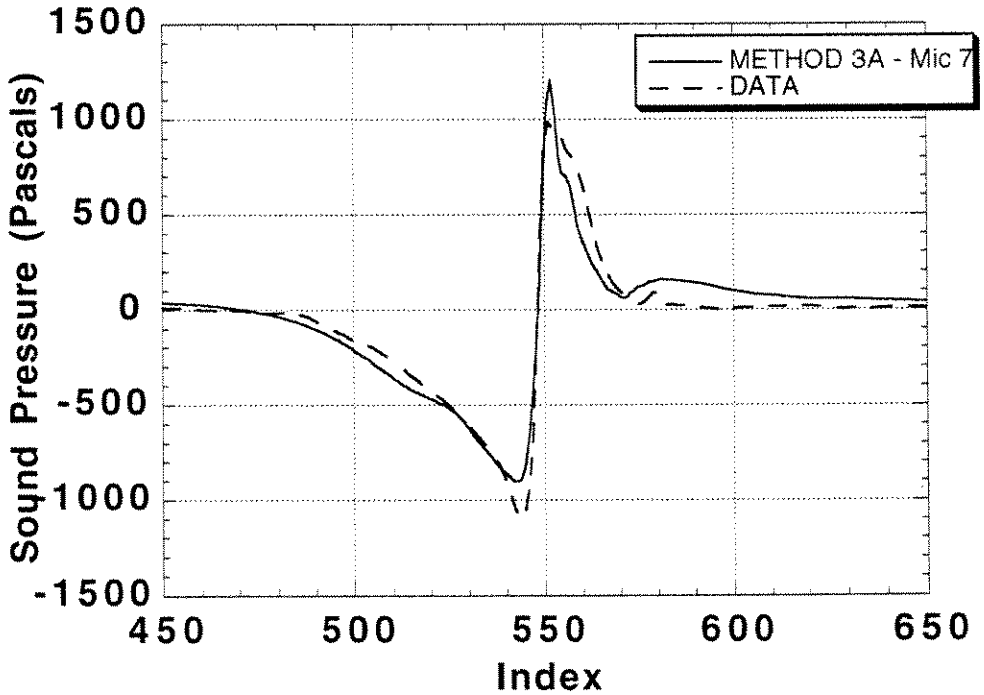

Figure 31b. Comparison of Method 3A computational results with experimental data at Microphone 7 for Case 1B.

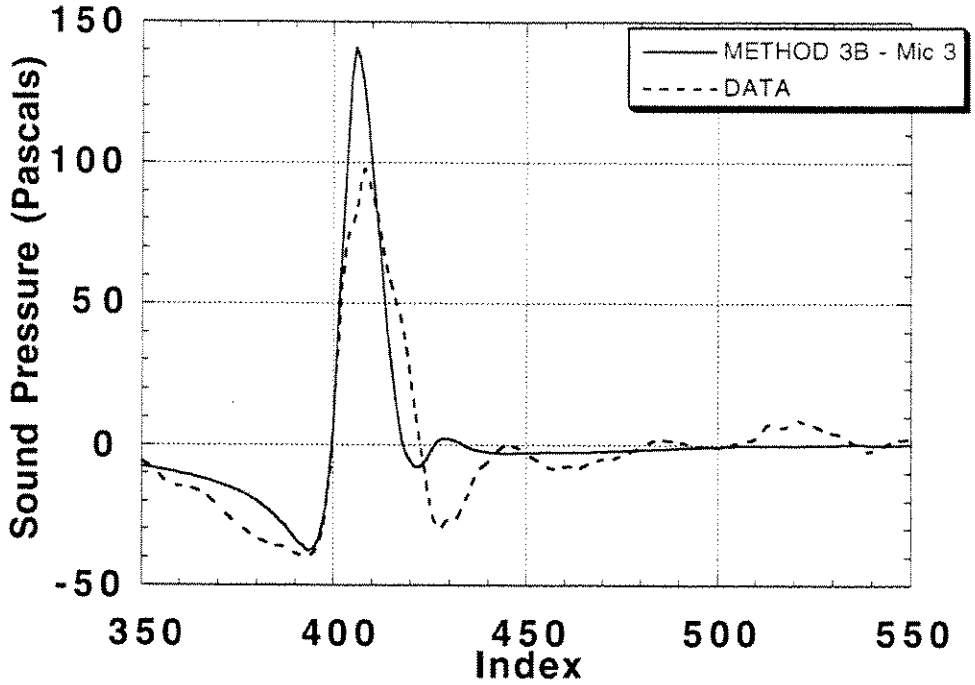

Figure 32a. Comparison of Method 3B computational results with experimental data at Microphone 3 for Case 1D.

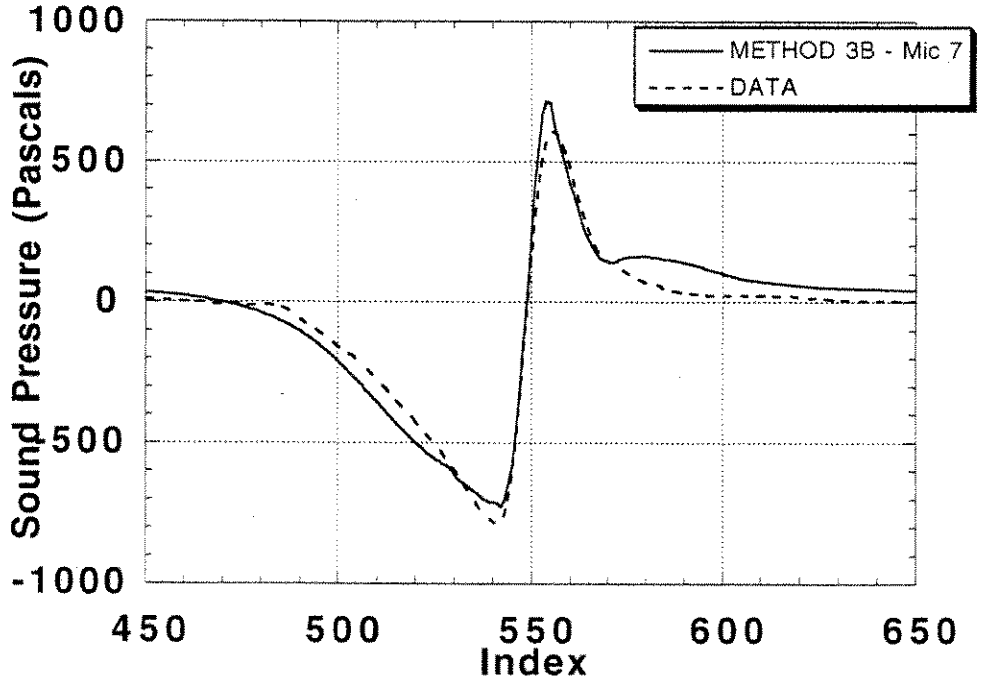

Figure 32b. Comparison of Method 3B computational results with experimental data at Microphone 7 for Case 1D.

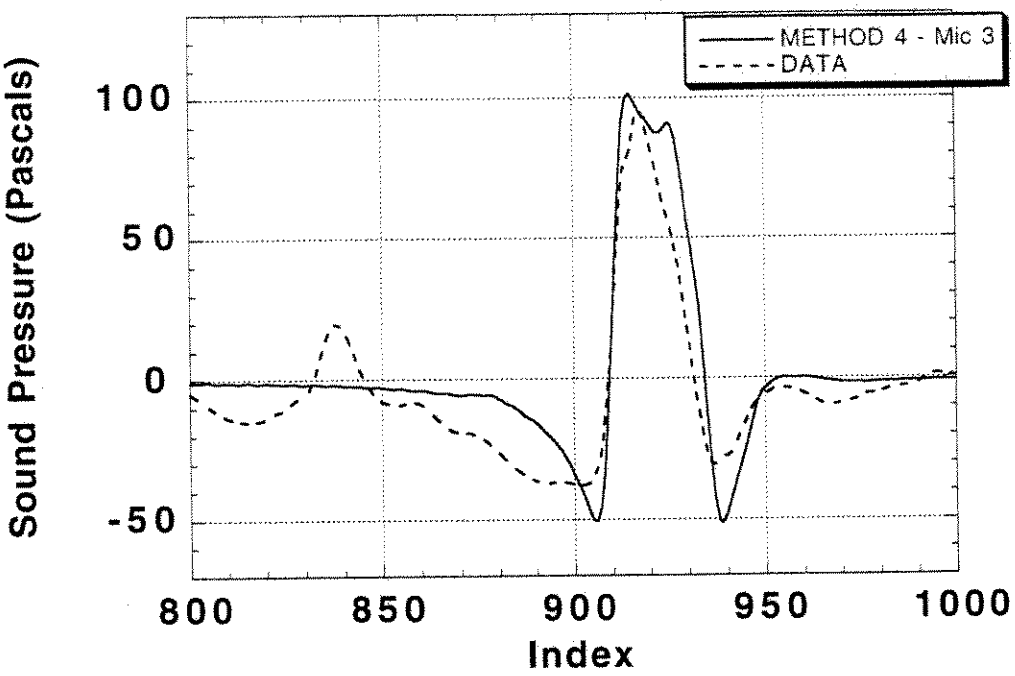

Figure 33a. Comparison of Method 4 computational results with experimental data at Microphone 3 for Case 1D.

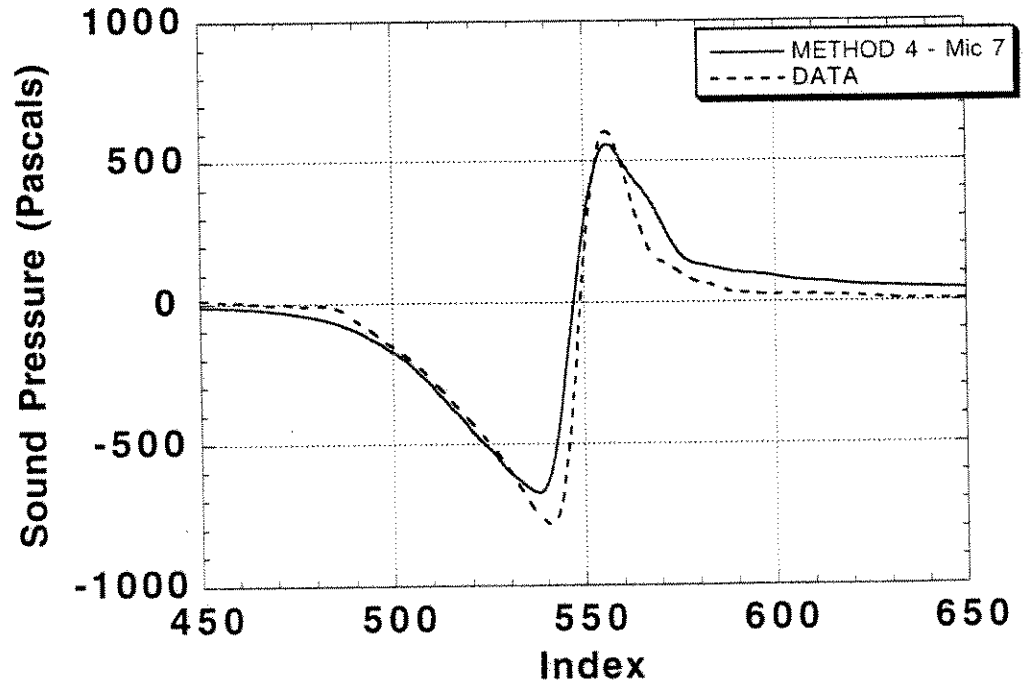

Figure 33b. Comparison of Method 4 computational results with experimental data at Microphone 7 for Case 1D.

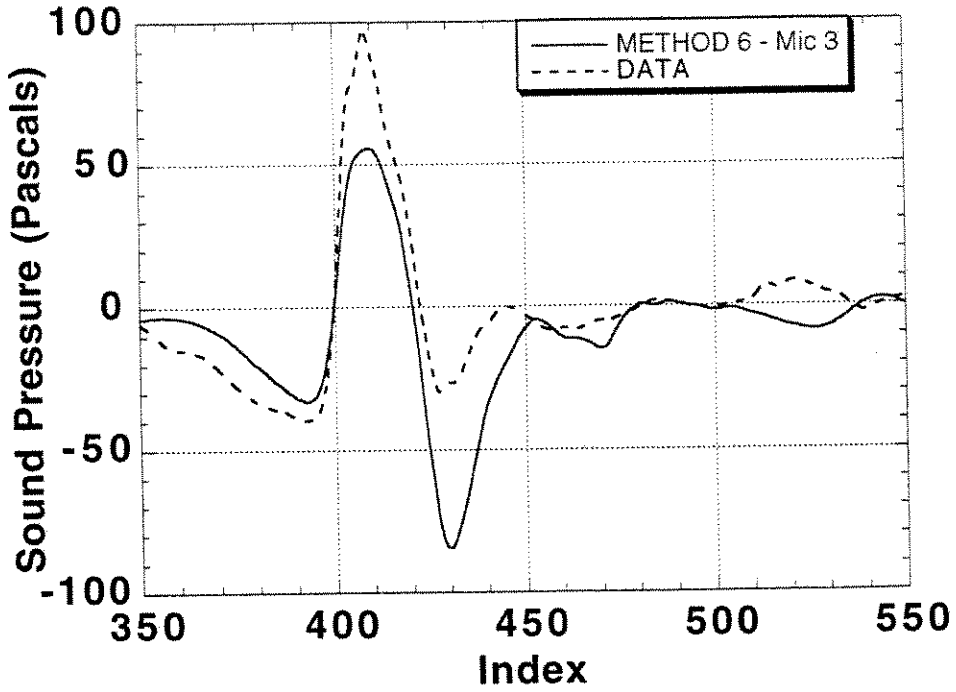

Figure 35a. Comparison of Method 6 computational results with experimental data at Microphone 3 for Case 1D.

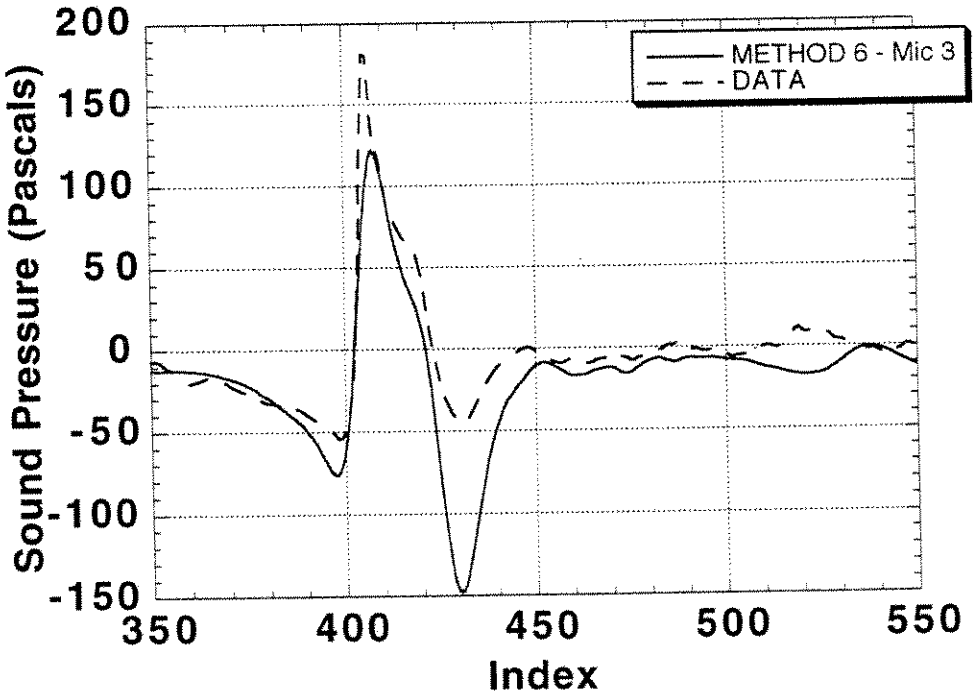

Figure 35b. Comparison of Method 6 computational results with experimental data at Microphone 3 for Case 1B.

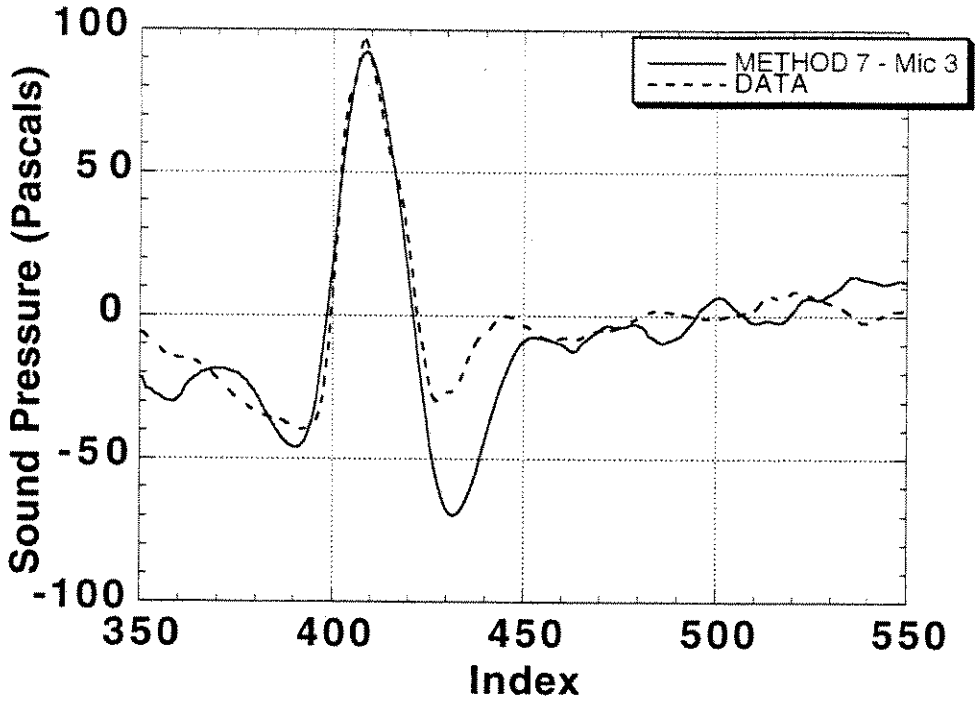

Figure 36a. Comparison of Method 7 computational results with experimental data at Microphone 3 for Case 1D.

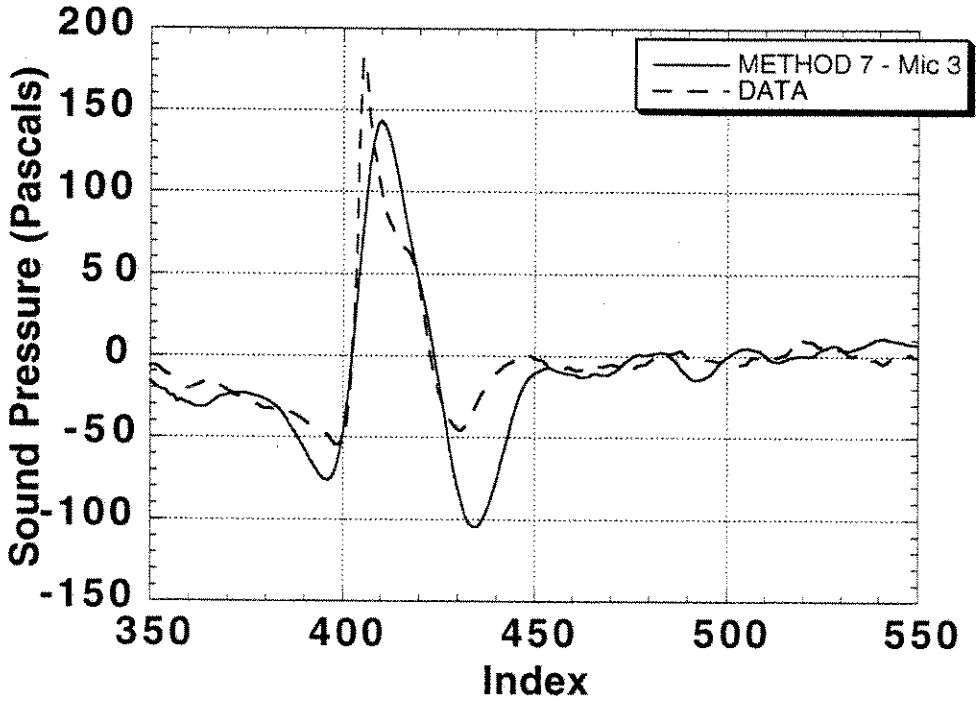

Figure 36b. Comparison of Method 7 computational results with experimental data at Microphone 3 for Case 1B.

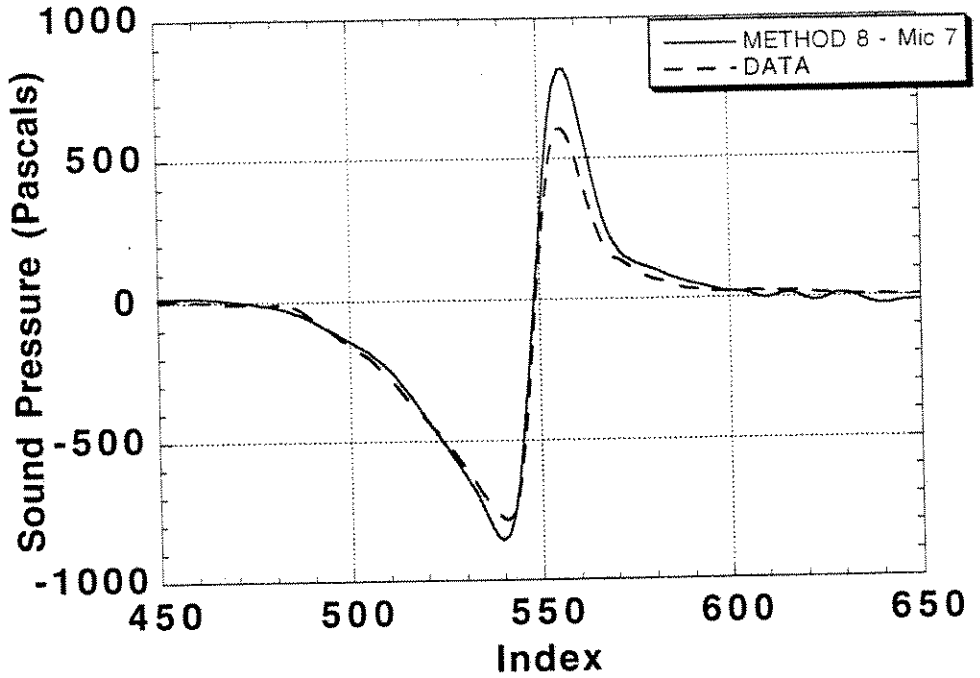

Figure 37. Comparison of Method 8 computational results with experimental data at Microphone 7 for Case 1D.

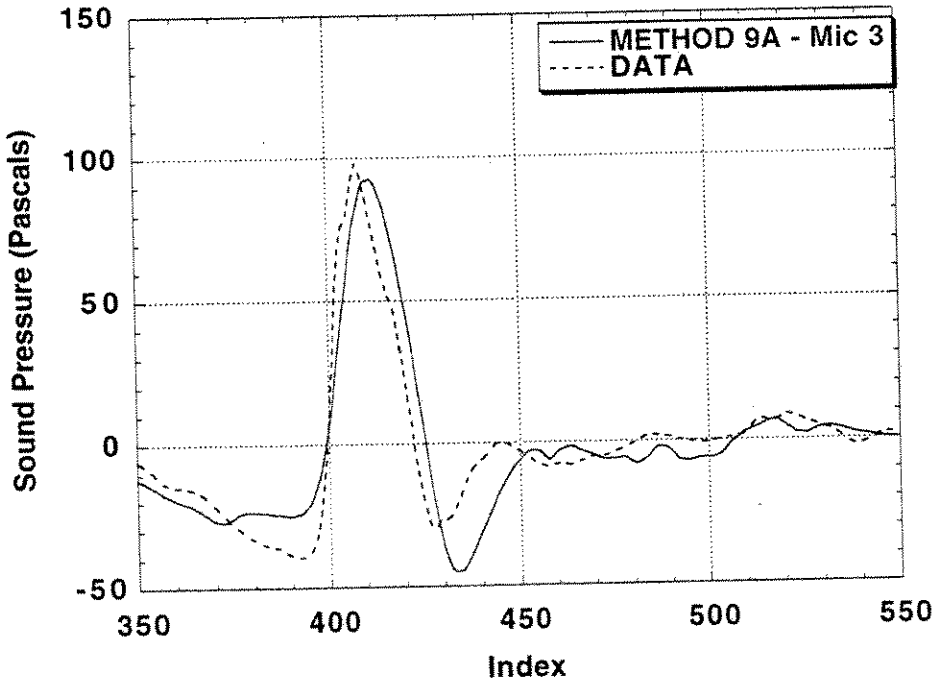

Figure 38a. Comparison of Method 9A computational results with experimental data at Microphone 3 for Case 1D.

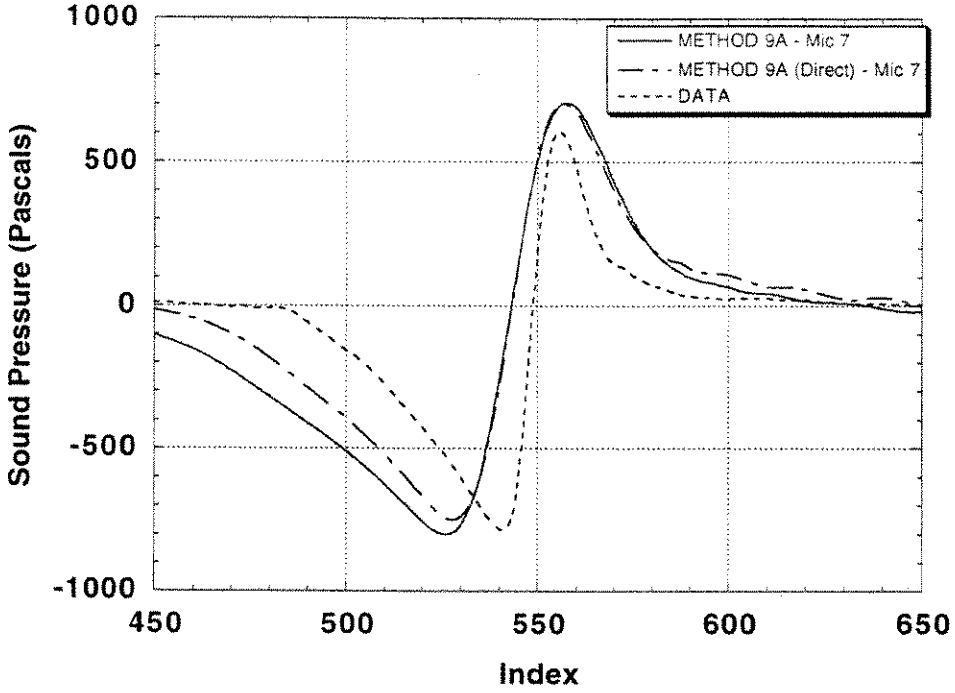

Figure 38b. Comparison of Method 9A computational results with experimental data at Microphone 7 for Case 1D.

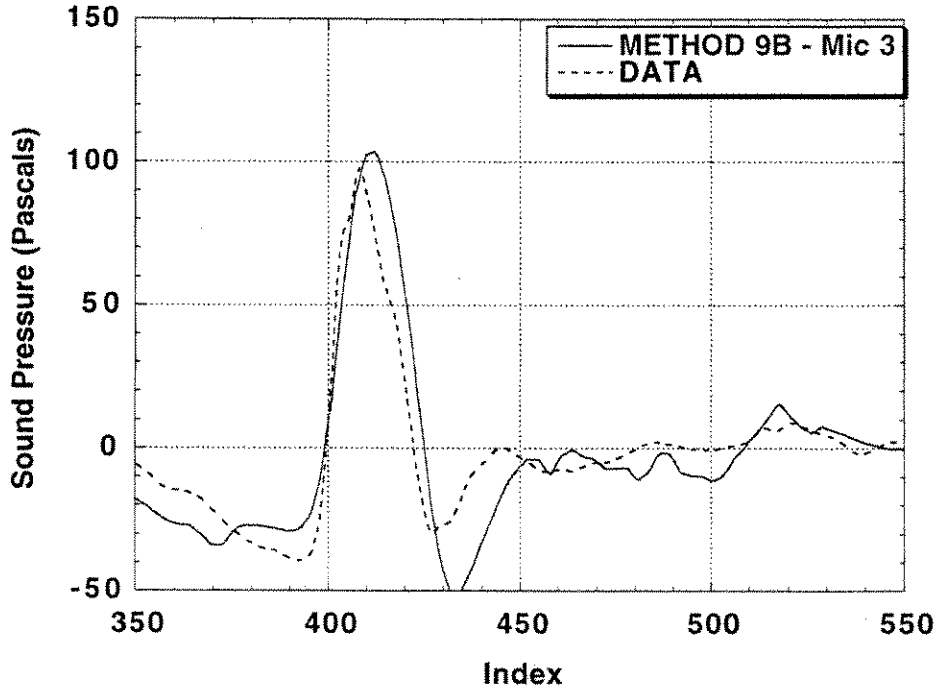

Figure 38c. Comparison of Method 9B computational results with experimental data at Microphone 3 for Case 1D.

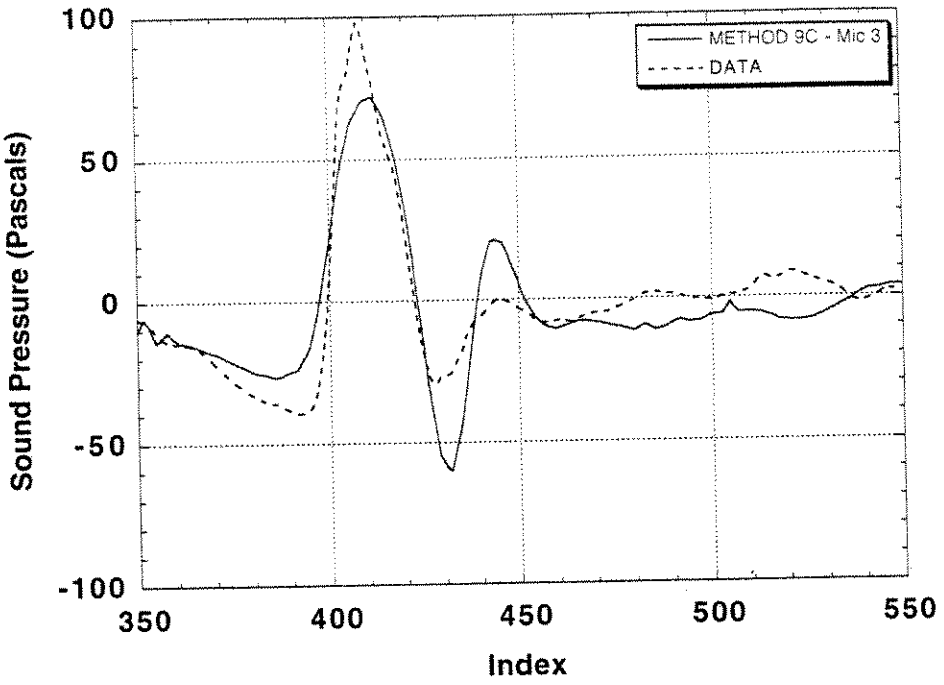

Figure 38d. Comparison of Method 9C computational results with experimental data at Microphone 3 for Case 1D.

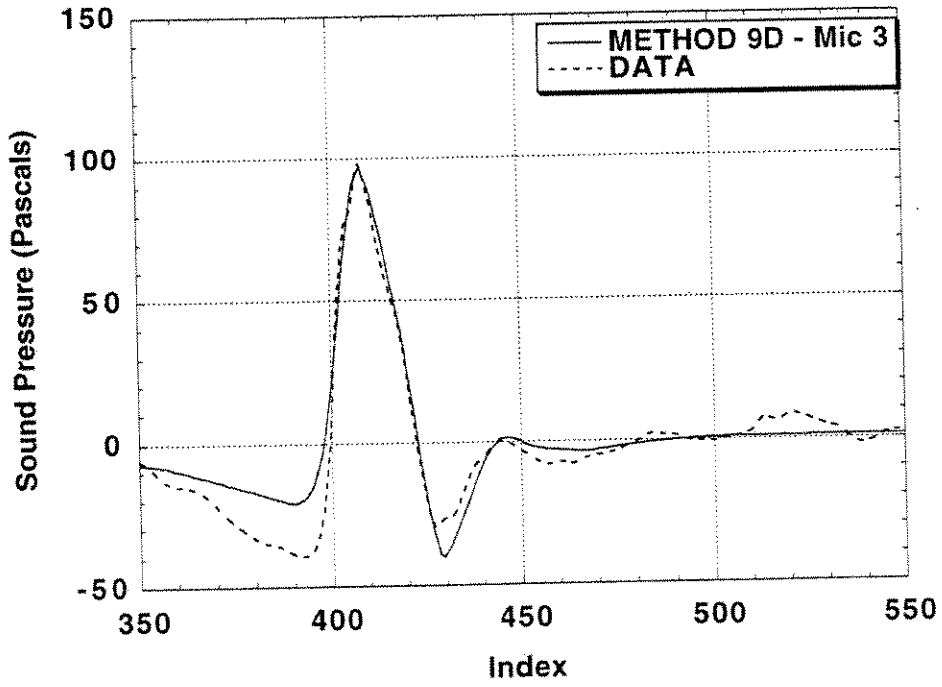

Figure 38e. Comparison of Method 9D computational results with experimental data at Microphone 3 for Case 1D.

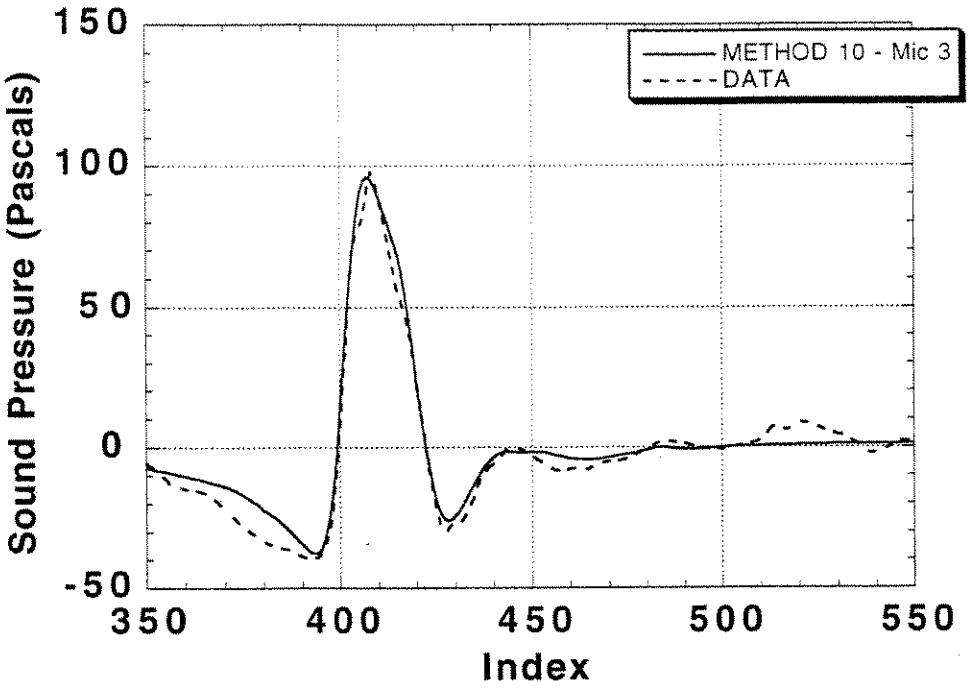

Figure 39a. Comparison of Method 10 computational results with experimental data at Microphone 3 for Case 1D.

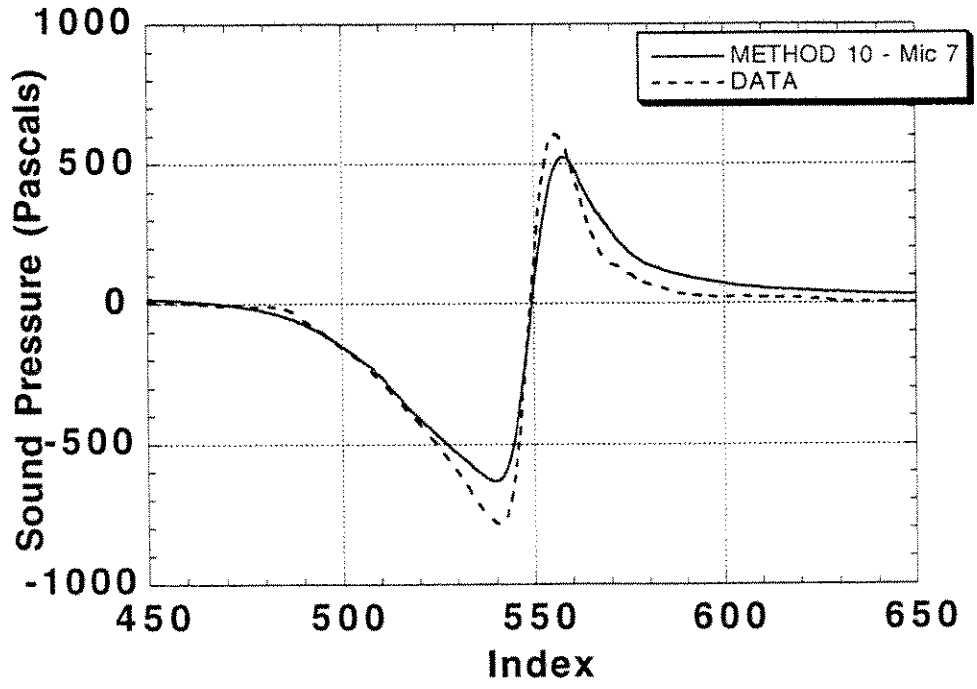

Figure 39b. Comparison of Method 10 computational results with experimental data at Microphone 7 for Case 1D.

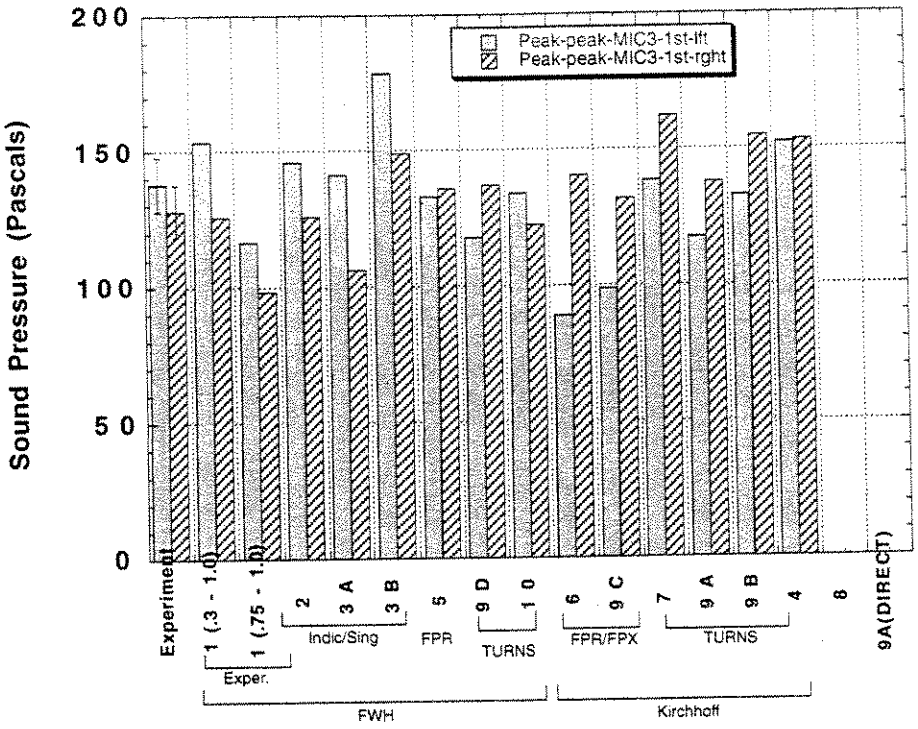

Figure 40a. Peak to peak acoustic pressure comparison for all methods for Microphone 3, Case 1D.

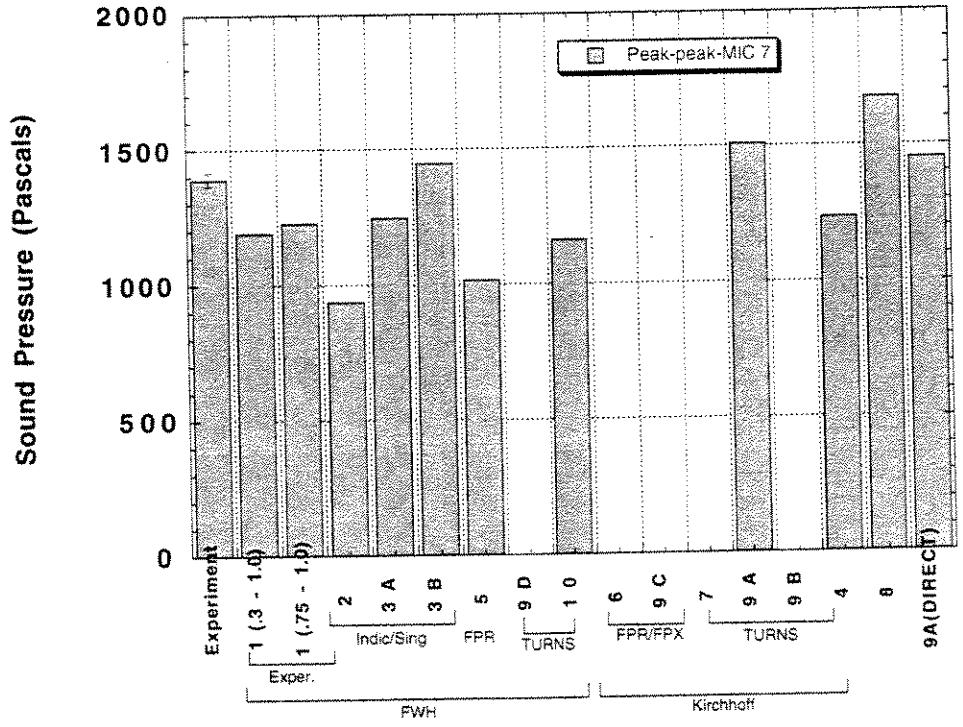

Figure 40b. Peak to peak acoustic pressure comparisons for all methods for Microphone 7, Case 1D